Localized perturbations in binary fluid convection with and without throughflow

P. Büchel and M. Lücke
Institut für Theoretische Physik, Universität des Saarlandes, Postfach 151150, D-66041 Saarbrücken, Germany
(Received 21 August 2000; published 21 December 2000)

Dynamics and structure of spatially localized convective perturbations in binary fluid layers heated from below and the effect of a plane horizontal Poiseuille throughflow on them are investigated. Fronts and pulse-like wave packets formed out of the three relevant perturbations—two oscillatory ones and a stationary one—are analyzed after evaluating the appropriate saddle points of the three respective dispersion relations of the linear field equations over the complex wave number plane. Front and pulse properties are elucidated in quantitative detail as a function of small throughflow Reynolds numbers for different Soret coupling strengths ψ including the pure fluid limit $\psi=0$ in comparison with the appropriate Ginzburg-Landau amplitude equation approximations. Furthermore, small amplitude pulses and fronts obtained from solving the full *nonlinear* field equations numerically are presented to check and compare with the linear results.

DOI: 10.1103/PhysRevE.63.016307 PACS number(s): 47.20.−k, 47.10.+g, 47.27.Te, 47.54.+r

I. INTRODUCTION

In forced nonequilibrium systems that undergo a pattern forming instability [1] the spatiotemporal evolution of spatially localized perturbations is of substantial practical, experimental, and theoretical interest. As long as the field amplitudes of the perturbation are small one can discard the effect of nonlinearities in the deviations from the unperturbed reference state. Then one can use a linear analysis to determine the behavior of such perturbations that often can be decomposed as linear wave packet superpositions of spatially extended Fourier modes. In particular when the packet contains modes that can grow one wants to determine the spatiotemporal evolution of the fronts that join the wave packet's intensity envelope to the unperturbed state as a function of control parameters and of the structural dynamics of the constituent pattern type. Here questions arise concerning the propagation velocities (and their directions) of the fronts, the spatial growth and decay behavior of the fronts, and the pattern selection induced under the moving fronts.

In this paper we investigate these problems theoretically for perturbations that occur in binary fluid mixtures heated from below [2,1] close to the primary stability and bifurcation thresholds [3–5] of the quiescent homogeneous conductive state. Its linear stability analysis shows that there are three different types of perturbations—and of course their superpositions—that depending on parameters can grow and thereby destroy the conductive state near threshold in this system: a stationary perturbation that has the structure of rolls which are fixed in space and two oscillatory perturbations in the form of traveling waves (TW's) where the phase of the roll pattern is propagating in opposite directions.

After the experimental observation [6] of transient, weakly nonlinear TW convection close to the oscillatory threshold also weakly nonlinear, so-called, counterpropagating waves were seen in rectangular convection channels [7,8] as superpositions of left and right propagating TW's that were reflected from the lateral sidewalls. Also so-called blinking states [7–10] were observed where the amplitude of a TW becomes alternatingly large at the sidewalls before being reflected with reduced amplitude [11,12,8]. Thus, the counterpropagating waves and the blinking state are strongly influenced by the system size and the reflection properties of the sidewalls [8,13]. On the other hand, freely moving linear wave packets of TW's were observed up to the time where they hit a sidewall [14] or collided with a strongly nonlinear, spatially localized convection pulse [15].

It should be noted that the aforementioned linear or weakly nonlinear convection phenomena differ substantially from the strongly nonlinear spatially extended and spatially localized convection states [16] showing large deviations [17,18] of the concentration distribution from the conductive state and they also differ from the erratic burst and decay of TW pulses [26] that has been called dispersive chaos [26].

In this paper we present a linear analysis of spatially localized convection fields thereby restricting ourselves to small perturbations of the conductive state. We determine and elucidate front and wave packet properties of the three relevant perturbation types and the influence of an externally imposed throughflow on them. This analysis is made for different strengths of the Soret coupling ψ between temperature and concentration fields including the pure fluid limiting case $\psi=0$. The analysis is based on a numerical evaluation of the complex dispersion relations over the complex wave number plane. These functions are determined for the different perturbation types using the full linearized field equations. But we also make quantitative comparisons with the appropriate Ginzburg-Landau amplitude equation (GLE) approximations for different ψ and different throughflow and with numerical simulations of the full nonlinear field equations.

It is somewhat surprising that such an analysis has not yet been performed in view of the fact that the two fronts that are bounding each of the three different packet types consisting of the three different perturbation types differ in general from each other. Thus, all in all there are six different fronts some of which are for special cases related to each other by symmetry operations. But even in the absence of any throughflow the spatiotemporal properties of the two fronts of a TW packet are different thus giving rise to a competition of different pattern selection and growth behavior at the two fronts. We hope that our analysis will help to shed more light

on the rather complex pattern growth processes that occur in binary mixture convection.

Our paper is organized as follows. In Sec. II we describe the system and we provide the theoretical framework for determining its linear properties. In Sec. III we briefly review the linear bifurcation behavior of different spatially extended convective patterns with and without external throughflow in order to provide the background and a frame for discussing later on spatially localized perturbations. In Sec. IV we evaluate with a saddle point analysis of the complex dispersion relations of the field equations and of the GLE approximations the boundaries in parameter space between convective and absolute instability in order to determine whether the two fronts of a particular wave packet type move in the same or into opposite directions. Section V deals with front and pulse behavior in mixtures ($\psi \neq 0$) and in pure fluids for zero and finite throughflow. Here we compare also for the different perturbation types the saddle point properties of the appropriate dispersion relations of the field equations with those of the GLE approximations. In order to check and to compare the spatiotemporal behavior of fronts and pulses following from the saddle point analysis of the dispersion relations of the *linear* field equations we present in Sec. V some representative results that were obtained from a numerical solution of the full *nonlinear* hydrodynamical field equations. Section VI contains a summary of the major results and in the Appendix we give details about the different numerical methods used here.

II. SYSTEM

We consider a horizontal layer of a binary fluid mixture like, e.g., alcohol-water confined between two parallel, perfectly heat conducting and impervious plates. The setup is exposed to a homogeneous gravitational field $\mathbf{g}=-g\mathbf{e}_z$ and a temperature gradient $\Delta \underline{T}=\underline{T}_{lower}-\underline{T}_{upper}$ between the lower and upper confining boundaries. Unscaled quantities are underlined to distinguish them from the scaled ones introduced below.

A. Field equations

The system is described by the balance equations for mass, heat, concentration, and momentum in Oberbeck-Boussinesq approximation [27,2]

$$0=-\boldsymbol{\nabla}\cdot\mathbf{u}, \tag{2.1a}$$

$$\partial_t T=-\boldsymbol{\nabla}\cdot\mathbf{Q}; \quad \mathbf{Q}=\mathbf{u}T-\boldsymbol{\nabla}T, \tag{2.1b}$$

$$\partial_t C=-\boldsymbol{\nabla}\cdot\mathbf{J}; \quad \mathbf{J}=\mathbf{u}C-L\boldsymbol{\nabla}(C-\psi T), \tag{2.1c}$$

$$\partial_t \mathbf{u}=-\boldsymbol{\nabla}(\mathbf{u}:\mathbf{u}+p-\sigma\boldsymbol{\nabla}u)+\mathbf{B}; \tag{2.1d}$$

$$\mathbf{B}=\sigma Ra(T+C)\mathbf{e}_z.$$

Lengths are scaled with the height d of the layer, time with the vertical thermal diffusion time d^2/κ, and the velocity field $\mathbf{u}=(u,v,w)$ with κ/d. Here, κ is the thermal diffusivity of the mixture; $T=(\underline{T}-\underline{T}_0)/\Delta\underline{T}$ denotes the scaled deviation of the temperature from the mean temperature $\underline{T}_0$ in the fluid. The field $C=(\underline{C}-\underline{C}_0)\beta/(\alpha\Delta\underline{T})$ is the scaled deviation of the mass concentration $\underline{C}=\underline{\rho}_1/(\underline{\rho}_1+\underline{\rho}_2)$ of the solute from its mean $\underline{C}_0$. Here $\underline{\rho}_1$ and $\underline{\rho}_2$ are the mass density fields of the two components. For small deviations of $\underline{T}$ and $\underline{C}$ from their means the total mass density $\underline{\rho}=\underline{\rho}_1+\underline{\rho}_2$ is governed by a linear equation

$$\underline{\rho}=\underline{\rho}_0[1-\alpha(\underline{T}-\underline{T}_0)-\beta(\underline{C}-\underline{C}_0)], \tag{2.2}$$

with α, β being the thermal and solutal expansion coefficient of the fluid, respectively. For ethanol-water mixtures at room temperature α and β are positive [28].

The Lewis number L is the ratio of concentration diffusivity D and thermal diffusivity κ, and the Prandtl number σ is the ratio of momentum diffusivity ν and κ:

$$L=\frac{D}{\kappa}; \quad \sigma=\frac{\nu}{\kappa}. \tag{2.3}$$

For room temperatures (10 °C−40 °C), the Prandtl number of ethanol-water mixtures lies between 5 and 20 [28], while for normal fluid Helium it is ten or more times smaller. The Lewis number of liquid mixtures is about 0.01. In this paper we take the fluid parameters $L=0.01$ and $\sigma=10$ as representative examples for ethanol-water mixtures.

The setup is characterized by three control parameters that can be varied independently:

(i) The Rayleigh number

$$Ra=\frac{\alpha g d^3}{\kappa\nu}\Delta\underline{T} \tag{2.4}$$

measures the externally imposed thermal driving due to the temperature gradient between the plates. For convenience we use the scaled Rayleigh number

$$r=\frac{Ra}{Ra_c^0} \tag{2.5}$$

that is reduced by the critical Rayleigh number Ra_c^0 for onset of convection in a pure fluid with the critical wave number k_c^0. The analytical values are $Ra_c^0=1707.762$ and $k_c^0=3.11632$.

(ii) The lateral throughflow driven by a lateral pressure gradient defines the Reynolds number

$$Re=\langle u\rangle_z\frac{d}{\nu} \tag{2.6}$$

where $\langle u\rangle_z$ is the vertical average of the lateral velocity field. We consider in this paper a throughflow in positive x-direction with positive Reynolds number.

(iii) The separation ratio

$$\psi=-\frac{\beta}{\alpha}\frac{k_T}{\underline{T}_0} \tag{2.7}$$

with the thermo diffusion ratio k_T of the mixture reflects the influence of temperature gradients on the concentration current $\mathbf{J}$.

For negative separation ratios ψ the imposed temperature gradient causes in the quiescent heat conducting state an antiparallel concentration gradient via the Soret effect. The resulting solutal contribution to the density change is opposite to the thermal contribution, thus weakens the buoyancy and stabilizes the heat conducting state. For room temperature ethanol-water mixtures, ψ-values between about -0.5 and $+0.2$ can be easily realized experimentally [28]. The Dufour effect that reflects the coupling of a concentration gradient into the heat current $\mathbf{Q}$ can be discarded in binary liquid mixtures [29,30]. The buoyancy force $(\rho-\rho_0)\mathbf{g}$ due to density deviations from the mean is the driving mechanism for convective motion. It enters into the momentum balance (2.1d) via the buoyancy term $\mathbf{B}$ which follows from (2.2) after scaling. This is the only place, where density variations are retained in Oberbeck-Boussinesq approximation. In the continuity equation (2.1a), the fluid has been assumed to be incompressible.

Rigid, impervious and perfectly heat conducting plates located at $z=\pm\frac{1}{2}$ define the horizontal boundary conditions

$$\mathbf{u}=0; \quad T=\mp\tfrac{1}{2} \text{ at } z=\pm\tfrac{1}{2} \tag{2.8}$$

for the fluid's velocity and temperature fields. Due to the impermeability of the plates there is no concentration current through the plates, $\mathbf{J}\cdot\mathbf{e}_z=0$, or

$$\partial_z C=\psi\partial_z T \text{ at } z=\pm\tfrac{1}{2}. \tag{2.9}$$

Since the pressure p is determined via a Poisson equation by $\mathbf{u}, T$, and C, we do not need boundary conditions for it.

B. Linear eigenvalue problem

For small Ra and Re a laterally homogeneous heat conducting state without convective vertical velocity is stable. In this basic state the velocity field $\mathbf{u}_{cond}=U(z)\mathbf{e}_x$ is given by the plane horizontal Poiseuille flow

$$U(z)=\sigma Re P(z)=\sigma Re 6(\tfrac{1}{4}-z^2); \tag{2.10}$$

temperature and concentration fields are linear functions in z

$$T_{cond}=-z; \quad C_{cond}=-\psi z. \tag{2.11}$$

The basis for our linear analysis of convective perturbations of the conductive state are the linearized field equations

$$(\partial_t-\sigma\boldsymbol{\nabla}^2)\boldsymbol{\nabla}^2 w+(U\boldsymbol{\nabla}^2-\partial_z^2 U)\partial_x w = \sigma Ra(\partial_x^2+\partial_y^2)[(1+\psi)\theta+\zeta], \tag{2.12a}$$

$$(\partial_t-\boldsymbol{\nabla}^2+U\partial_x)\theta=w, \tag{2.12b}$$

$$(\partial_t-L\boldsymbol{\nabla}^2+U\partial_x)\zeta=-\psi\boldsymbol{\nabla}^2\theta \tag{2.12c}$$

for the deviations

$$w, \quad \theta=T-T_{cond}, \quad \zeta=C-C_{cond}-\psi\theta \tag{2.13}$$

from the conductive state (2.10),(2.11). Here w is the vertical velocity field that vanishes in the conductive state. To derive Eq. (2.12a) we have applied twice the curl operator to Eq. (2.1d) using (2.1a). Note that the Poiseuille flow profile $U(z)$ enters into Eqs. (2.12) making them nonautonomous.

The horizontal boundary conditions for the convective perturbation fields w, θ, and ζ are

$$\theta=w=\partial_z w=\partial_z\zeta=0 \text{ at } z=\pm\tfrac{1}{2}. \tag{2.14}$$

Assuming the system to be laterally unbounded the general solution of the perturbation equations (2.12) can be written as a superposition of plane waves with horizontal wavevector

$$\mathbf{k}=k_x\mathbf{e}_x+k_y\mathbf{e}_y. \tag{2.15}$$

The plane-wave solution ansatz for the fields $\Phi=(w,\theta,\zeta)$ reads

$$\Phi(\mathbf{r},t)=\hat{\Phi}(z)e^{i(k_x x+k_y y)}e^{st} \tag{2.16}$$

with a complex characteristic exponent

$$s=\Re s+i\Im s=\gamma-i\omega \tag{2.17}$$

and complex z-dependent amplitude functions $\hat{\Phi}=(\hat{w},\hat{\theta},\hat{\zeta})$.

Inserting the ansatz (2.16) into the field equations (2.12) yields the 3×3 linear eigenvalue problem

$$(\mathcal{L}+s\mathcal{M})\hat{\Phi}(z)=0 \tag{2.18a}$$

for the eigenvalues s and eigenvectors $\hat{\Phi}$ with

$$\mathcal{L}=\mathcal{L}^{(0)}+i\sigma k_x Re\mathcal{L}^{(1)}, \tag{2.18b}$$

$$\mathcal{L}^{(0)}=\begin{pmatrix} -\sigma(\partial_z^2-k^2)^2 & \sigma Ra(1+\psi)k^2 & \sigma Rak^2 \\ -1 & k^2-\partial_z^2 & 0 \\ 0 & \psi(\partial_z^2-k^2) & L(k^2-\partial_z^2) \end{pmatrix}. \tag{2.18c}$$

Into

$$\mathcal{L}^{(1)}=\begin{pmatrix} P(\partial_z^2-k^2)-\partial_z^2 P & 0 & 0 \\ 0 & P & 0 \end{pmatrix}, \tag{2.18d}$$

enters the vertical profile $P(z)$ (2.10) of the Poiseuille throughflow and its second derivative. Finally

$$\mathcal{M}=\begin{pmatrix} \partial_z^2-k^2 & 0 & 0 \\ 0 & 1 & 0 \\ 0 & 0 & 1 \end{pmatrix}. \tag{2.18e}$$

In the absence of throughflow $\mathcal{L}$ reduces to $\mathcal{L}^{(0)}$. Due to the boundary conditions at the plates the eigenvalue spectrum is discrete. We are interested in characteristic exponents s whose eigenfunctions $\hat{\Phi}(z)$ have no nodes other than at the horizontal boundaries $z=\pm1/2$ which have growth rates γ that are closest to zero.

Since the horizontal wavevector $\mathbf{k}$ of the perturbation (2.16) and the throughflow Reynolds number Re enter into Eq. (2.12) only as k^2 and $k_x Re$ the dependence of the functions $f=s,\hat{\Phi}$ on $\mathbf{k}$ and Re is

$$f=f(k^2,k_x Re). \tag{2.19}$$

Using this behavior the Squire transformation [31]

$$f(k_x^2+k_y^2,k_x Re)=f(\tilde{k}_x^2,\tilde{k}_x\widetilde{Re}), \tag{2.20a}$$

$$\tilde{k}_x^2=k_x^2+k_y^2; \quad \widetilde{Re}=\frac{k_x}{\tilde{k}_x}Re \tag{2.20b}$$

relates the functions f for a wavevector with arbitrary components k_x,k_y to the functions that have been determined for wavevectors $\tilde{\mathbf{k}}=\tilde{k}_x\mathbf{e}_x$ in throughflow direction and Reynolds numbers $\widetilde{Re}$. The linear behavior of general perturbations with k_x,k_y can be obtained from the result for $\tilde{k}_x$ and $\widetilde{Re}$ with Eq. (2.20). Therefore we investigate here only convective perturbations with wavevectors in x-direction. In experiments they give rise to straight rolls which can most easily be seen in convection channels that are long in x-direction and narrow in y-direction.

III. SPATIALLY EXTENDED STRUCTURES

In this section we briefly review the influence of throughflow on linear bifurcation properties of different *spatially extended* convective patterns that have spatially homogeneous amplitudes [32]. These properties provide the background and a frame for discussing in the main part of this paper our findings on the behavior of *spatially localized* perturbations. We focus here our interest on small Reynolds numbers. For sufficiently large Re, the lowest relevant bifurcation threshold of binary mixtures with any ψ asymptotically approaches the critical Rayleigh number of pure fluid convection [32] since in this limit the externally imposed shear flow effectively eliminates the Soret-induced coupling effects between the convective concentration field and the other fields by suppressing vertical convective transport of Soret driven concentration perturbations.

A. Absence of throughflow

The stability properties of the conductive state against infinitesimal convective perturbations in the absence of throughflow have been discussed in detail in the literature [3–5,33]. For ψ above (below) the tricritical value $\psi_{SOC}^t=-O(10^{-7})$ [33], the stationary bifurcation to the so-called SOC state is forward (backward). However, below $\psi_{SOC}^\infty=-L/(1+L)$ [34,35] where the stationary threshold r_{stat} diverges, the lower SOC solution branch is disconnected from the conductive solution for positive r [36]. In addition there exists for strong stabilizing Soret coupling a Hopf bifurcation threshold at r_{osc} where symmetry-degenerated left and right traveling wave solutions branch out of the conductive state. The Hopf frequency ω_H varies as $\omega_H^2 \approx -449\psi/(1+\psi+1/\sigma)$ [37,9]. For ψ above (below) the tricritical value $\psi_{TW}^t=-O(10^{-4})$ [33,38] the TW bifurcation is forwards (backwards). The bifurcation thresholds r_{stat} and r_{osc} become equal at the codimension-two value $\psi_{CTP}=-O(10^{-5})$ with slightly different critical wave numbers and a small Hopf frequency. For a more detailed discussion of the codimension-two point see, e.g., [3–5,33,36].

B. Notation

Instead of numbering the three different bifurcation thresholds and bifurcating convective solutions of the 3×3 eigenvalue problem (2.12) in the presence of throughflow, $Re>0$, we use henceforth superscripts S,U,D. They identify the behavior of critical perturbations, $e^{i(k_c x-\omega_c t)}$, in the limit $Re\to0$. Eigenvalues for which $\omega_c(Re\to0)=0$ are marked by S, since these perturbations are stationary for $Re=0$. Eigenvalues for which $\omega_c(Re\to0)$ is positive (negative) carry the superscript D (U), since they characterize perturbations which propagate in downstream (upstream) direction for $Re\to0$. Thus, the cases S (''stationary''), D (''downstream''), and U (''upstream'') characterize the perturbations and with it the bifurcating nonlinear solutions in the limit $Re\to0$. For convenience we use this notation also in the absence of throughflow, $Re=0$. Then $D(U)$ identifies a TW where the phase is propagating to the right (left) with frequency $\omega^D>0$ ($\omega^U<0$).

Finally we should like to draw the attention to the fact that we distinguish the propagation direction of different TW's by their frequency not by their wavevector — we only consider positive $k_x=k$ in this work.

C. Effect of throughflow on the oscillatory instability

We briefly review in this subsection critical properties of a binary mixture like ethanol-water with $\psi=-0.25$ as a representative case for moderately negative Soret couplings. In the absence of throughflow, the threshold of stationary convection has already disappeared since $\psi>\psi_{SOC}^\infty=-L/(L+1)$. There exists only the Hopf bifurcation threshold at $r_{osc}=1.3348$ for symmetry degenerate left or right propagating TW's with the critical Hopf frequency $\omega_H=11.2125$. Finite throughflow breaks the symmetry of the two TW patterns and different, up- and downstream propagating TW's bifurcate out of the conductive state. They will be referred to as TWU (traveling wave upstream) and TWD (traveling wave downstream).

The relative difference between the critical wave numbers k_c^D and k_c^U of the D and U waves, repectively, is not more than a few percent for the mixtures and Reynolds numbers considered here. The critical frequencies ω_c^D and ω_c^U are practically linear functions of Re. They start at zero throughflow with the Hopf values ω_H and $-\omega_H$, respectively, and they can be very well approximated by the first-order result of a low-Re expansion [32]

$$\omega_c^{D,U}=\pm\omega_H+41.9Re. \tag{3.1}$$

The rate of change $\partial\omega_c/\partial Re\simeq41.9$ also holds for other separation ratios [32] including the pure fluid case [39].

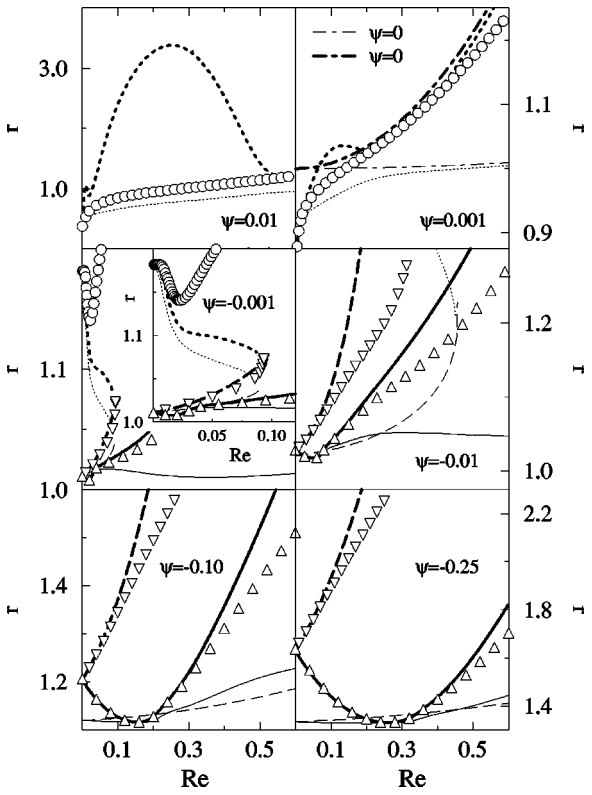

FIG. 1. Borderlines r_{c-a} between absolute and convective instability and stability curves r_c versus throughflow rate according to [32]. Symbols and *thick* curves represent r_{c-a} obtained from the full field equations and from the GLE, respectively. *Thin* curves show bifurcation thresholds r_c for spatially extended structures as discussed in Sec. III. Different types of perturbations are identified by circles and dotted lines (S), upwards pointing triangles and full lines (U), and downwards pointing triangles and dashed lines (D). The case of a pure fluid, $\psi=0$, is shown by dash-dotted lines: thick one for r_{c-a}^S and thin one for r_c^S. Parameters are $L=0.01, \sigma=10$, and ψ as shown.

Note that for $Re \geqslant \omega_H/41.9$ both critical frequencies, ω_c^D and ω_c^U, as well as the phase velocities $v_{ph}^{D,U}=\omega_c^{D,U}/k_c^{D,U}$ are positive. Then both critical waves propagate in throughflow direction in the laboratory frame. However, v_{ph}^U is always smaller — by about $2\omega_H/k_c(Re=0)$ — than v_{ph}^D. Only for $Re \leqslant \omega_H/41.9$ the phase velocity v_{ph}^U is negative and opposite to the throughflow. So, the wording ''upstream traveling waves'' does not necessarily imply that the phase velocity of such a TW is negative in the laboratory frame. It would be negative in a frame moving in throughflow direction with a conveniently defined mean lateral velocity like, e.g., $\overline{v}=\frac{1}{2}(v_{ph}^U+v_{ph}^D)$.

D. Bifurcation thresholds at negative ψ

Here we discuss the bifurcation thresholds r_c^U (thin, solid lines), r_c^D (thin, dashed lines), and r_c^S (thin, dotted lines) as functions of Re for a few characteristic negative Soret couplings as shown in Fig. 1.

1. $r_c^U(Re,\psi)$

With increasing throughflow rates, r_c^U (thin, solid lines in Fig. 1) decreases for small Re, develops a minimum close to where ω_c^U goes through zero, steeply increases thereafter, and finally flattens asymptotically for any Soret coupling ψ towards the Re-dependent pure fluid stability boundary $r_c(Re,\psi=0)$ at large Re. The flattening of r_c^U can be seen in Fig. 1 for the weaker Soret couplings $\psi=-0.001,-0.01$. With increasing Soret strength the flattening of r_c^U towards $r_c(Re,\psi=0)$ shifts to larger and larger Re [32] outside the plot range of Fig. 1. Thus a sufficiently large throughflow eliminates the Soret induced coupling effects between concentration field on one side and temperature and velocity field on the other side. For small ψ, e.g., at $\psi=-0.001$, the stability boundary r_c^U lies always below r_c^D while for larger $|\psi|$ there are two intersections of the curves r_c^U and r_c^D with $r_c^D \leqslant r_c^U$ in between [32]. Note, however, that the bicritical upstream and downstream TW perturbations can not be superimposed linearly to a standing wave since their wave numbers $k_c^U \neq k_c^D$ differ and furthermore $\omega_c^U \neq -\omega_c^D$. So in the Re-interval between the bistable intersections of r_c^D and r_c^D downstream propagating convection waves grow first while outside this interval at small Re and large Re TWU convection bifurcates first out of the conductive state.

2. $r_c^D(Re,\psi)$

The bifurcation threshold r_c^D (thin, dashed lines in Fig. 1) always increases monotonically with Re. The initial slope $\partial r_c^D/\partial Re$ increases somewhat with decreasing $|\psi|$. For $\psi=-0.01$ the stability curves r_c^D and r_c^S collide in the Re-range displayed in Fig. 1. For higher throughflow rates there opens up a wave number gap where neither D nor S perturbations can grow [32,40].

3. $r_c^S(Re,\psi)$

In pure fluids, $\psi=0$, the bifurcation threshold $r_c(Re,\psi=0)$ (thin, dashed-dotted line in right, top part of Fig. 1) slightly increases with growing Re [39]. In binary mixtures with negative Soret coupling, on the other hand, the stationary threshold r_c^S (thin, dotted lines in Fig. 1) gets very strongly depressed by a small throughflow. In the absence of throughflow r_c^S rapidly increases with $|\psi|$ and diverges at $\psi_{SOC}^\infty=-L/(L+1)$. Beyond this Soret coupling the solution branch of stationary nonlinear convection is disconnected from the basic state as $r_c^S(Re=0,\psi \leqslant \psi_{SOC}^\infty)=\infty$. A small but finite throughflow, however, moves the threshold r_c^S down to finite values: The dotted line for r_c^S of Fig. 1 for $\psi=-0.01 < \psi_{SOC}^\infty$ shows (i) that $r_c^S=\infty$ below a finite $Re_\infty \simeq 0.019$, (ii) that r_c^S is finite for $Re>Re_\infty$, and (iii) that r_c^S steeply drops down for $Re>Re_\infty$ [32]. The Reynolds number Re_∞ where r_c^S diverges grows with increasing $|\psi|$ — a stronger Soret coupling requires a larger throughflow to move the bifurcation threshold r_c^S from infinity to a finite value.

IV. TRANSITION BETWEEN CONVECTIVE AND ABSOLUTE INSTABILITY

Whenever at a stability threshold the frequency is nonzero with a finite group velocity

$$v_g = \left.\frac{\partial \omega(k)}{\partial k}\right|_{k_c} \tag{4.1}$$

one has to distinguish between spatiotemporal growth behavior of spatially *extended* and of spatially *localized* perturbations. The former having a form $\sim e^{ik_c x}$ have a positive growth rate above the bifurcation thresholds r_c determined in the previous section.

A. Wave packets

Due to the rotational invariance of the fluid layer in the $x-y$ plane without throughflow there is no preferred wavevector direction for the growth of infinitesimal perturbations out of the basic state. Consequently one observes in experimental setups with large extensions $\Gamma_x, \Gamma_y \gg 1$ in x- and y-direction, respectively, for strong stabilizing Soret couplings a growth dynamics of TW perturbations that is quite complex in space and time [41–43]. However, in narrow convection cells, say, with $\Gamma_y \simeq 1-3$ and large Γ_x or in narrow annular convection channels the roll axes are oriented parallel to the smaller side of the cell and the wave vectors are oriented in x-direction. Here we shall not investigate the competition [44,45] between logitudinal rolls and transversal rolls with wavevectors in x-direction and y-direction, respectively, that occurs in wider systems in the presence of a throughflow.

Consider first a spatially localized, infinitesimal perturbation of the basic state that contains only one type of TW's, e.g., right traveling waves with different wave numbers. So this is a linear superposition, i.e., a wave packet, of TWD's. Above the threshold of instability, $r > r_{osc}$, the projection of the initial perturbation onto the eigenfunctions of the critical mode grows exponentially within the framework of the linearized field equations, whereas any contributions from modes with higher threshold values and more complicated vertical field structure are strongly damped. Furthermore, for small $|r - r_{osc}|$ only contributions with wave numbers in the narrow band above the marginal stability curve $r^{TW}_{stab}(k)$ can grow whereas other contributions are damped. After fast transients have decayed a pulse like perturbation of TWD's survives with wave numbers within the unstable band centered around the wave number of maximal growth $k^{TW}_{max} \simeq k^{TW}_c$. The center of such a pulse propagates approximatively with the linear group velocity, v_g (4.1), which can be determined via a standard linear stability analysis. Such pulses have also been investigated experimentally, e.g., by Kolodner *et al.* [14]. Due to reflection at the lateral sidewalls of rectangular channels exponentially growing pulses can end up in blinking states for very small overcritical Rayleigh numbers [8,9,13,14,46–49].

Since the above described wave packet contains TWD's that can grow the pulse will grow as well. However, there are two parameter regimes to be distinguished. (i) In the so-called connectively unstable parameter regime [50,51] the wave packet moves with the velocity v_g faster away than it grows — while growing in the frame comoving with v_g the pulse moves out of the system so that the basic conductive state is restored. In other words, the two fronts that join the wave packet's intensity envelope to the structureless state propagate both in the direction in which the packet center moves. (ii) In the so-called absolutely unstable parameter regime the growth rate of the packet is so large that one front propagates in the laboratory frame to the center motion. Thus, the packet expands not only into the direction of the pulse motion but also opposite to it [50] so that eventually the initial perturbation can fill the entire system.

We should like to emphasize that we are dealing here only with a linear analysis of the convective fields. Thus we do not address the question whether the above described wave packet grows to a stable nonlinear state that then might expand back into the system with a larger negative nonlinear front velocity so that the nonlinear structured state ultimately invades the region occupied by the homogeneous state although the latter is linearly not absolutely unstable [52,53].

B. Saddle point analysis

The boundary in parameter space between convective and absolute instability is marked by parameter combinations for which one of the fronts of the linear wave packet reverts its propagation direction in the laboratory frame: In the convectively unstable regime this front propagates in the same direction as the center of the packet, in the absolutely unstable regime it moves opposite to it, and right on the boundary between the two regimes the front is stationary in the laboratory frame. This parameter combination can be determined by a saddle point analysis of the linear complex dispersion relation $s(Q)$ over the pane of complex wave numbers [51]

$$Q = \Re Q + i \Im Q = k - iK. \tag{4.2a}$$

Here we do not display the dependence of

$$s(Q) = \Re s(Q) + i \Im s(Q) = \gamma(Q) - i\omega(Q) \tag{4.2b}$$

on r, Re, ψ, L, σ and we also do not indicate that in binary mixtures with throughflow one has to consider three different dispersion relations for the three different perturbations of type S, U, and D as explained in Sec. III.

The condition of vanishing front propagation velocity is equivalent to finding the parameters for which

$$\Re s(Q^*) = \gamma(Q^*) = 0 \tag{4.3a}$$

with Q^* denoting the appropriate saddle position of $s(Q)$ in the complex wave number plane given by $[ds(Q)/dQ]|_{Q^*} = 0$. Using the Cauchy-Riemann relations for the analytic function $s(Q)$ this saddle condition amounts to

$$\left.\frac{\partial \gamma(Q)}{\partial k}\right|_{Q^*} = 0, \quad \left.\frac{\partial \gamma(Q)}{\partial K}\right|_{Q^*} = 0. \tag{4.3b}$$

The solution of Eq. (4.3) yields the sought after boundary between convectively and absolutely unstable parameter regimes. Quantities on this boundary are identified henceforth by the subscript $c-a$.

To solve Eqs. (4.3) we evaluate the z dependent eigenfunctions $\hat{\Phi}(Q,z,s)$ that solve the eigenvalue problem (2.18) for fixed σ, L, ψ, Re, r, Q, and an initial guess for $s=\gamma-i\omega$. With two staggered Newton algorithms we first iteratively adjust s in order to fulfill the boundary conditions at the plates and then change r, k, and K such as to match the conditions of Eqs. (4.3). In addition we solved the eigenvalue problem also with a Galerkin expansion (Appendix) for the z dependent eigenfunctions. Then we used the more convenient formulation

$$\gamma=0, \quad \mathcal{D}=0, \quad \frac{\partial \mathcal{D}}{\partial Q}=0 \tag{4.4}$$

of Eqs. (4.3) in terms of the implicit formulation (Appendix) $\mathcal{D}(\sigma,L,\psi,Re,r,Q,s)=0$ of the dispersion relation in order to determine $k_{c\text{-}a}$, $K_{c\text{-}a}$, $r_{c\text{-}a}$, and $\omega_{c\text{-}a}$ [40].

C. Ginzburg-Landau amplitude equation approximation

To determine the boundary between convective and absolute instability via the solution of Eqs. (4.3) requires knowledge of the dispersion relation $s(Q;r,Re,\psi)$ for complex Q. So one has to solve the eigenvalue problem (2.18) for complex Q which is a quite involved numerical task. A somewhat simpler, yet approximate method, is to use an expansion of $s(Q;r,Re,\psi)$ around the critical point, $Q_c=k_c, r=r_c$, that corresponds to approximate the full linear field equations by the linear Ginzburg-Landau amplitude equation (GLE). We recapitulate the relevant equations [32] here for completeness. The comparison with results from the full field equation (Sec. IV D) shows that the GLE yields quite useful approximations to the borderlines between absolute and convective instability.

Consider Re and ψ to be fixed for the moment so that we do not have to display them explicitly in the argument list of s. Under the assumptions (i) that the sought after saddle Q^* in the complex Q plane lies close to the critical wave number k_c of the respective perturbation type and (ii) that the relative distance

$$\mu_{c-a}=\frac{r_{c-a}}{r_c}-1 \tag{4.5}$$

between the convective/absolute border r_{c-a} and the critical Rayleigh number r_c is small we expand

$$s(Q;r)=s_c+(Q-k_c)\left(\frac{\partial s}{\partial Q}\right)_c+\frac{1}{2}(Q-k_c)^2\left(\frac{\partial^2 s}{\partial Q^2}\right)_c + \mu\left(r\frac{\partial s}{\partial r}\right)_c+\text{h.o.t.} \tag{4.6}$$

Here we have introduced for convenience the relative distance

$$\mu=\frac{r}{r_c}-1 \tag{4.7}$$

of the Rayleigh number r from its critical value r_c for onset of convection which in general depends on Re,ψ,σ, and L. The higher order terms in Eq. (4.6) should be of order $\mu^{3/2}$ since for small $0<\mu\ll 1$ only extended perturbations with (real) wave numbers out of a band of width $k-k_c\sim\sqrt{\mu}$ can grow.

The expansion coefficients of Eq. (4.6) appear also in the linear parts of the complex GLE

$$\tau_0(\partial_t+v_g\partial_x)A=[(1+ic_0)\mu+(1+ic_1)\xi_0^2\partial_x^2]A + \text{nonlinear terms.} \tag{4.8a}$$

Here $A(x,t)$ is the common complex amplitude of convection fields $\Phi=(w,\theta,c)$

$$\Phi(x,z,t)=A(x,t)\hat{\Phi}(z)e^{i(k_c x-\omega_c t)}+\text{c.c.} \tag{4.8b}$$

that bifurcate out of the conductive state at $\mu=0$. The approximation (4.8) can be expected to be a good one as long as A is small and, more importantly, as long as the spatial field structure is well represented by that of the critical eigenfunctions $\hat{\Phi}(z)e^{ik_c x}$.

The relations between the expansion coefficients of s and the coefficients in the amplitude equation are

$$\left(\frac{\partial s}{\partial Q}\right)_c=-i\left(\frac{\partial \omega}{\partial Q}\right)_c=-iv_g, \tag{4.9a}$$

$$\left(r\frac{\partial s}{\partial r}\right)_c=r_c\left(\frac{\partial \gamma}{\partial r}-i\frac{\partial \omega}{\partial r}\right)_c=\frac{1+ic_0}{\tau_0}, \tag{4.9b}$$

$$\left(\frac{\partial^2 s}{\partial Q^2}\right)_c=-\frac{2\xi_0^2}{\tau_0}(1+ic_1). \tag{4.9c}$$

In Eq. (4.9c) we have used

$$\left(\frac{\partial^2 \gamma}{\partial k^2}\right)_c=-\left(\frac{\partial \gamma}{\partial r}\frac{\partial^2 r_{stab}}{\partial k^2}\right)_c \tag{4.10}$$

to relate the second k derivative of the growth rate to the critical curvature $\xi_0^2=\frac{1}{2}(\partial^2 r_{stab}/\partial k^2)_c$ of the marginal stability curve $r_{stab}(k)$. The approximated dispersion relation (4.6)

$$\tau_0[s+i\omega_c+iv_g(Q-k_c)] =(1+ic_0)\mu-(1+ic_1)\xi_0^2(Q-k_c)^2 \tag{4.11}$$

is precisely the one of the GLE approximation (4.8) to the linear fields (w,c,θ).

Note that the dispersion (4.6) and with it the coefficients τ_0,v_g,c_0,c_1,ξ_0 (4.9) of the amplitude equation, the amplitude $A(x,t)$, the eigenfunctions $\hat{\Phi}(z)$, and the critical quan-

tities k_c, ω_c, r_c all carry a superscript S, U, or D that identifies the kind of perturbation considered.

With the notation (4.9) the saddle Q^* of the approximated dispersion (4.6) lies at

$$Q^* = k_c - \frac{i}{1+ic_1}\frac{v_g\tau_0}{2\xi_0^2}. \tag{4.12}$$

Then the condition (4.3a) yields the GLE approximation

$$\mu_{c-a} = \frac{v_g^2\tau_0^2}{4\xi_0^2(1+c_1^2)}, \tag{4.13a}$$

$$r_{c-a} = (1+\mu_{c-a})r_c \tag{4.13b}$$

for the boundary between the convectively and absolutely unstable parameter regime [51,54].

D. Results

In this section we present results related to the border between convective and absolute instability. They were obtained with the saddle point analysis of (i) the numerically obtained dispersion relations of the full linear field equations (Appendix) and (ii) of their GLE approximations. Quantities on the border between convective and absolute instability are marked by the subscript $c-a$.

1. Pure fluid convection as a test case

To test our numerical procedure we have investigated the pure fluid limiting case of vanishing Soret coupling, $\psi = 0$. We have determined the values k_{c-a}, K_{c-a}, r_{c-a}, and ω_{c-a} [55,45] as functions of the Peclet number

$$Pe = \sigma Re. \tag{4.14}$$

In Fig. 2 we show results determined with the shooting method (Appendix) using a spatial discretization of 1/500 and 1/1000 for $\sigma = 0.1$, 1, 10, and $\sigma \to \infty$.

It is easy to see that the results are independent under the combined symmetry operations

$$Pe \to -Pe, \quad K_{c-a} \to -K_{c-a}, \quad \omega_{c-a} \to -\omega_{c-a}. \tag{4.15}$$

So K_{c-a} and ω_{c-a} are linear functions and k_{c-a} and μ_{c-a} are quadratic functions in lowest order of Pe [45]. Within the GLE approximation the symmetry (4.15) is reflected by the fact that c_0, c_1, and v_g are odd functions in Pe whereas τ_0 and ξ_0^2 are even functions.

2. Binary mixtures: Convective and absolute instability for S,U, and D perturbations

In binary fluid mixtures the Hopf bifurcation of TW's generates already in the absence of throughflow finite group velocities. Therefore, there exists also for $Re = 0$ a transition between convective and absolute instability when increasing

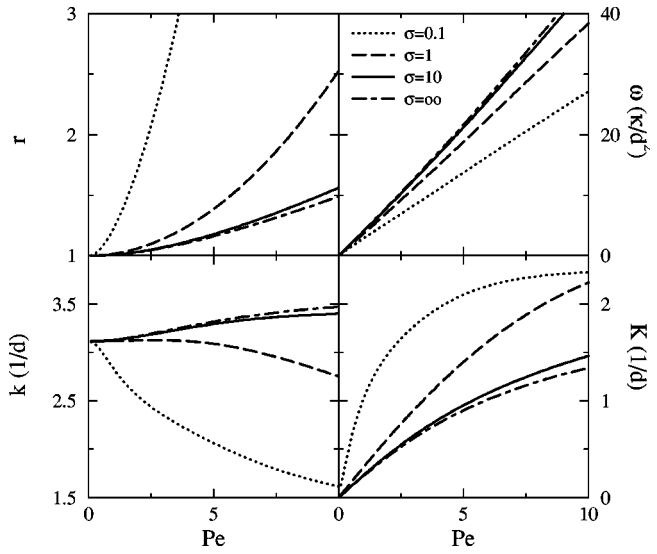

FIG. 2. Saddle point results for wavepackets at the transition between convective and absolute instability in pure fluid convection ($\psi = 0$) as a function of throughflow Peclet number $Pe = \sigma Re$ for several Prandtl numbers σ as indicated. Shown are r_{c-a}, ω_{c-a}, k_{c-a}, and K_{c-a} as obtained from determining the dispersion $s(Q)$ of the full field equations with a shooting method.

r. In the absence of throughflow k_{c-a} and μ_{c-a} are identical for left and right traveling waves whereas K_{c-a} and ω_{c-a} have opposite sign.

In the presence of throughflow the symmetry degeneracy between left and right traveling waves is lifted and one has to distinguish between the three different types of extended, propagating perturbations, namely S, U, and D, against which the basic conductive state becomes unstable at the bifurcation thresholds r_c^S, r_c^U, and r_c^D [32]. Consequently one has to investigate the spatiotemporal growth behavior of three different wave packets consisting of superpositions of TWS, TWU, or TWD plane wave perturbations.

The set of these three eigenfunctions and eigenvalues of Eq. (2.18) transforms into each other upon reverting the throughflow direction, i.e., under the operation $Re \to -Re$ since the hydrodynamic field equations are invariant under the parity operation $(x,u) \to -(x,u)$ with u being the velocity field in x-direction. The transformation behavior [32] of $\{s^S, s^U, s^D; \hat{\Phi}^S, \hat{\Phi}^U, \hat{\Phi}^D\}$ follows explicitly from the fact that the linear operator $\mathcal{L}$ entering the eigenvalue equation (2.18) transforms as $\mathcal{L}(-k_x Re) = \mathcal{L}^*(k_x Re)$ under $Re \to -Re$ with the star denoting here complex conjugation. Here we do not display the other arguments of $\mathcal{L}$ that remain unchanged. The transformation behavior [32] of the dispersion relations s^S, s^U, s^D under the operation $Re \to -Re$ imply relations between $\{r,k,K,\omega\}_{c-a}^{S,U,D}$ for Re and $-Re$ [40].

In Fig. 1 we present the boundaries r_{c-a}^S (circles), r_{c-a}^U (upwards pointing triangles), and r_{c-a}^D (downwards pointing triangles) between convective and absolute instability of the basic state against type S, U, and D perturbations as functions of Re for different Soret coupling strengths [32]. These results have been obtained from the saddle point analysis of the respective dispersion relations over the complex Q-plane

which themselves were determined with the shooting method (Appendix) using a spatial resolution of 1/3000 and 1/6000.

In order to determine these three boundaries within the GLE approximation we have determined the derivatives (4.9) of the respective eigenvalues s^S, s^U, and s^D at their respective critical points $r_c(Re,\psi)$, $k_c(Re,\psi)$. Then Eq. (4.13) yields the functions $r_{c-a}(Re,\psi)$ for the three patterns. They are shown in Fig. 1 by thick lines (S: dotted, U: full, D: dashed) together with the corresponding bifurcation thresholds r_c (thin lines). Especially for stabilizing Soret couplings, $\psi>0$, and small Re the GLE approximation is very close to the numerically exact results, however, with too large slopes at higher throughflow rates.

Within the GLE approximation one obtains a local maximum of r^S_{c-a} (e.g., at $\psi=0.01$, $Re\simeq 0.25$ and at $\psi=0.001$, $Re\simeq 0.1$) when the product of τ_0, which decreases with Re, and v_g, which increases with Re, reaches a maximum. For $\psi=0.01$ a second maximum is visible at small Re that is possibly associated with a root of c_1. In contrast r^S_{c-a} resulting from the full field equations (circles) is monotonously increasing with Re. This strong deviation in r^S_{c-a} for positive ψ between GLE and full analysis is caused by the strong Re dependence of the coefficients of the amplitude equation [32].

For the negative Soret couplings of Fig. 1 r^U_{c-a} first decreases with increasing Re, coincides at its local minimum with r^U_c when $v_g=0$, and afterwards increases with Re. Hence, at fixed r one encounters with increasing Re first a transition from convective to absolute instability against TWU perturbations. Then, upon increasing Re further, one leaves the absolutely unstable region again to enter again a convectively unstable regime. The consequences following from this functional form of the border line r^U_{c-a} on the behavior of TWU fronts are discussed in Sec. VI B 2. The GLE approximation yields good quantitative agreement with the results of the full field equations for r^U_{c-a} (upwards pointing triangles) in the vicinity of the local minimum, while for higher Re the GLE results increase more strongly with Re. For smaller Reynolds numbers the validity range of the GLE result is typically enlarged down to $Re=0$ for the ψ-values presented here.

We have limited our investigation of r^D_c and r^S_c as functions of Re to cases, where the wave number gap in the $D-S$ marginal stability curves [32,40] has not yet appeared. Therefore, within the GLE approximation r^D_{c-a} and r^S_{c-a} are determined by the expansion coefficients of s (4.9) at the critical Rayleigh number r_c only as long as the calculation of r^D_c and r^S_c was numerically possible. Nevertheless, for higher Re critical Rayleigh numbers still exist to the left and right hand side of the wave number gap. We also found that the S saddle point of the full field equations (evaluated by successively increasing Re) evolves monotonously when Re increases beyond the threshold where the wave number gap occurs. The wave number of this saddle point increases with Re.

The GLE results for r^D_{c-a} are increasing stronger than those of the full field equations (downwards pointing triangles). For $\psi=-0.001$ the r^D_{c-a} stability limit seems to terminate close to the Reynolds number where the wave number gap opens up in the $D-S$ marginal stability curves. There K^* seems to change sign when increasing Re further. A graphical analysis of this saddle that has moved into the lower complex Q-plane suggests that there $\Re s<0$ above a certain Re-limit for all r so that this saddle can be ignored.

V. FRONTS AND PULSES

In view of the fact that the literature on linear fronts and pulses is quite extensive — cf. the review of Cross and Hohenberg [1] for a concise example — we give here only the theoretical background that is necessary for understanding our results. The fronts that we are investigating here and that appear also as constituents of pulses are perturbations of the basic state where the fields (locally) have the form

$$f(x,t)\sim e^{s(Q)t}e^{iQx}=e^{[\gamma(Q)-i\omega(Q)]t}e^{i[k-iK]x}. \qquad (5.1)$$

Here $Q=k-iK$ as in the previous section and $s(Q)=\gamma(Q)-i\omega(Q)$ is the linear complex dispersion relation of the field equations over the plane of complex wave numbers Q.

A. Notation

Here we introduce the notation for the six different linear fronts of the form (5.1) that we discuss in this paper. The envelope of Eq. (5.1) varies as e^{Kx}. So when $K>0$ the perturbation (5.1) grows at $x=-\infty$ out of the basic state. We call such a front to be of type $+$ and identify the associated front properties by a subscript $+$. On the other hand, for $K<0$ we have a front of type—with an intensity envelope of the perturbation (5.1) that joins at $+\infty$ with the basic state; see Fig. 3 for schematic plots. So the two subscripts $\pm$ identify the *spatial* variations of the front profiles. A pulse-like perturbation of the quiescent state would consist sufficiently away from its center of a $+$ front to the left and of a $-$ front to the right of the pulse center.

The *dynamical* properties of the constituent perturbations (5.1) under a front envelope are identified by superscripts S, U, and D as explained in Sec. III B, as used in Sec. IV D, and as indicated schematically in Fig. 3. The three different dynamical properties combined with the two different spatial profiles yield six different fronts. For convenience we use the superscripts U and D also for the case $Re=0$ without throughflow to identify left or right traveling waves, respectively. The throughflow with $Re>0$ is always understood to be directed in positive x-direction. So, for example, k^D_+ denotes the real wave number of a TWD-pattern whose phase propagates in downstream direction under a front of type $+$ with a spatial growth $\sim e^{K^D_+ x}$. The velocity v^D_+ of this front might be positive or negative. So in the case of $v^D_+>0$ ($v^D_+<0$) this front moves downstream (upstream). The time evolution of, e.g., the width of a pulse consisting, say, of TWD perturbations then depends on the magnitude and sign of the velocities v^D_+ and v^D_- of its left and right fronts, repectively.

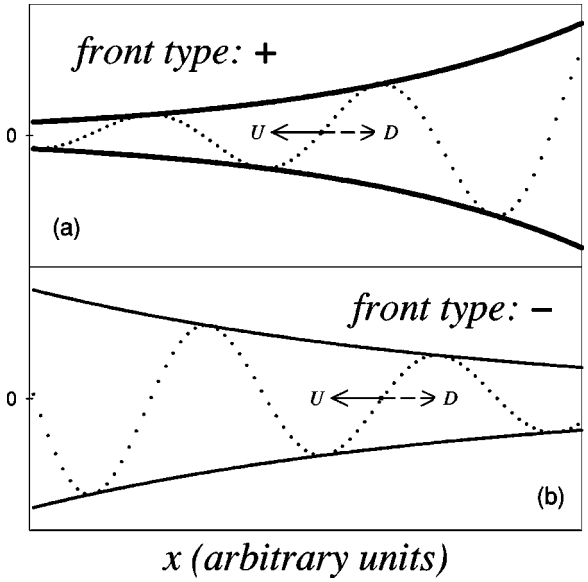

FIG. 3. Schematic plot of different fronts. Thick full lines in (a) and thin full lines in (b) show intensity envelopes of + type and of − type fronts connecting to the quiescent basic state at $x\to-\infty$ and at $x\to\infty$, respectively. Dots denote the actual TW structure growing under the front: a TWU perturbation (marked by *U* and a full arrow) propagates upstream to the left and a TWD perturbation (marked by *D* and a dashed arrow) moves downstream to the right. These conventions, dashed lines for TWD patterns, full lines for TWU patterns, thick lines for + fronts, and thin lines for − fronts are used also later on in Figs. 5 and 6.

B. Saddle point analysis

The analysis of linear fronts is based upon an investigation of the spatiotemporal properties of spatially localized perturbations

$$f(x,t)=\int_{-\infty}^{\infty}\frac{dk}{2\pi}e^{ikx}f(k,t=0)e^{s(k)t} \tag{5.2}$$

that consist of a wave packet superposition of spatially extended waves with real wave number k [1]. Each wave contributes to Eq. (5.2) with the weight $f(k,t=0)$ being the smooth Fourier transform of a sufficiently localized initial perturbation $f(x,t=0)$ and evolves according to its dispersion $s(k)$. To find the (linearly selected) long-time front propagation behavior of such a perturbation under a front that connects the perturbation to the basic state and that propagates with velocity v one analyzes

$$f(x=vt,t)=\int_{-\infty}^{\infty}\frac{dk}{2\pi}e^{[s(k)+ivk]t}f(k,t=0) \tag{5.3}$$

in the frame comoving with the front. In the limit of $t\to\infty$ the integral (5.3) is evaluated after deforming the original integration path along the real k-axis into the complex wave number plane via the dominant contribution from the relevant saddle point Q^* given by

$$\frac{d}{dQ}[s(Q)+ivQ]|_{Q=Q^*}=0. \tag{5.4a}$$

The condition that the temporal growth rate of the front vanishes in the frame comoving with the front velocity v^* implies the relation

$$0=\Re[s(Q)+ivQ]|_{Q=Q^*}=\gamma(Q^*)+v^*K^*. \tag{5.4b}$$

We combine Eqs. (5.4a) and (5.4b) into the three equations

$$v^*=-\frac{\gamma(Q^*)}{K^*}=-\left.\frac{\partial\gamma(Q)}{\partial K}\right|_{Q^*};\quad \left.\frac{\partial\gamma(Q)}{\partial k}\right|_{Q^*}=0 \tag{5.4c}$$

that we have solved. The solution of these three equations yields the three quantities Q^* and v^*. In the laboratory frame the spatiotemporal structure of the field under the front determined by Eq. (5.4) has the form

$$f(x,t)\sim e^{i(k^*x-\omega^*t)}e^{K^*(x-v^*t)}. \tag{5.5}$$

Thus the saddle conditions (5.4) determine all spatiotemporal properties of the front: velocity v^*, spatial growth rate K^*, wave number k^*, and frequency ω^*.

Investigations of the linear front dynamics within the GLE approximation showed that front solutions with $|K|>|K^*|$ were unstable against the marginally stable front determined by the saddle Q^* of the GLE dispersion relation [56–60]. So here we have a universal long-time dynamical selection of the marginally stable front solution that holds almost independently from the form of the localized initial perturbation [58,1]. For this reason and in order to compare later on with results obtained from the full field equation we first compile in Sec. V C the known front properties following from the GLE.

C. Ginzburg-Landau amplitude equation approximation

The saddle point analysis of Sec. V B applied to the dispersion relation (4.11) of the GLE (4.8) yields the following front properties;

$$\xi_0K_\pm^*=\pm\sqrt{\frac{\mu}{1+c_1^2}}, \tag{5.6a}$$

$$k_\pm^*-k_c=-c_1K_\pm^*, \tag{5.6b}$$

$$v_\pm^*-v_g=-2(1+c_1^2)\frac{\xi_0^2}{\tau_0}K_\pm^*, \tag{5.6c}$$

$$\gamma_\pm^*=-v_\pm^*K_\pm^*, \tag{5.6d}$$

$$\tau_0(\omega_\pm^*-\omega_c)=\tau_0v_g(k_\pm^*-k_c)+(c_1-c_0)\mu \tag{5.6e}$$

for the two front types with $K_+^*>0$ and $K_-^*<0$, respectively. They are associated with the two saddles of Eq. (5.4) that arise from the quadratic dispersion relation (4.11). At the boundary μ_{c-a} (4.13a) between convective and absolute in-

stability the velocity v_+^* and the temporal growth rate γ_+^* of the + front vanish in the laboratory frame. Then $v_-^*=2v_g$ and $\gamma_-^*=v_g^2\tau_0/\xi_0^2(1+c_1^2)$ are the velocity and the growth rate, respectively, of the − front. Thus, the center of the pulse-like perturbation moves with the group velocity v_g such that at μ_{c-a} its left front remains fixed and its right front moves with velocity $2v_g$. In the convecively unstable regime $0<\mu<\mu_{c-a}$ both the left front as well as the right front of the pulse move into the same (downstream) direction, $0<v_+^*<v_-^*$. In the absolutely unstable regime $\mu>\mu_{c-a}$, however, the left front moves upstream and the right front moves downstream, $v_+^*<0<v_-^*$.

Note that *all* quantities in Eq. (5.6) and in the ensuing discussion carry also the superscript S,U, or D which, however, is not displayed in Eq. (5.6) for the sake of shortness. These superscripts identify the phase dynamics of the respective perturbation under the front (cf. Sec. V B). The coefficients of the three associated amplitude equations entering into Eq. (5.6) have been evaluated as a function of ψ,Re in [61]. The limiting case, $\psi=0$, of pure fluid convection is contained also in Eq. (5.6).

D. Fronts in pure fluids—comparison of GLE and field equations

We have first investigated as a test case the pure fluid limiting case of vanishing Soret coupling, $\psi=0$, in the absence of throughflow, $Re=0$. Then $\mu=\epsilon=r/r_c-1$ with $r_c(Re=0,\psi=0)=1$. Here we compare the front properties of stationary roll convection perturbations growing under the fronts obtained from the field equations with those from the GLE. The latter yields according to Eq. (5.6) in the absence of throughflow for a stationary pattern the well known results [1]

$$\xi_0 K_\pm^* = \pm\sqrt{\epsilon};\quad k_\pm^* = k_c, \tag{5.7a}$$

$$v_\pm^* = \mp 2\frac{\xi_0}{\tau_0}\sqrt{\epsilon};\quad \gamma_\pm^* = 2\frac{\epsilon}{\tau_0};\quad \omega_\pm^* = 0 \tag{5.7b}$$

since $c_0=c_1=v_g=\omega_c=0$ for pure fluids without throughflow. For this system one has $\xi_0=0.385$ and $\tau_0=(\sigma+0.5117)/19.65\sigma$ for rigid horizontal boundary conditions [1].

This GLE result (thin lines in Fig. 4) is in reasonable good agreement with the linear front properties that we evaluated for a wide range of Prandtl numbers σ from the dispersion of the full field equations by a shooting method (thick lines in Fig. 4). Corrections to the r-independent GLE values of $k_\pm^*=k_c$ and $\omega_\pm^*=0$ are of higher order that are not captured by the GLE. Since ξ_0 is independent of σ so is K^*. But v^* depends on σ via τ_0.

Note that according to the full field equations the perturbation (5.5) that is growing under the moving front shows a phase propagation with phase velocity ω^*/k^* that is in general nonzero while the GLE yields $\omega^*=0$. The question of whether there is a phase propagation under a convection front of perturbations that grow beyond the stationary instability of pure fluids seems to be a somewhat open question [62].

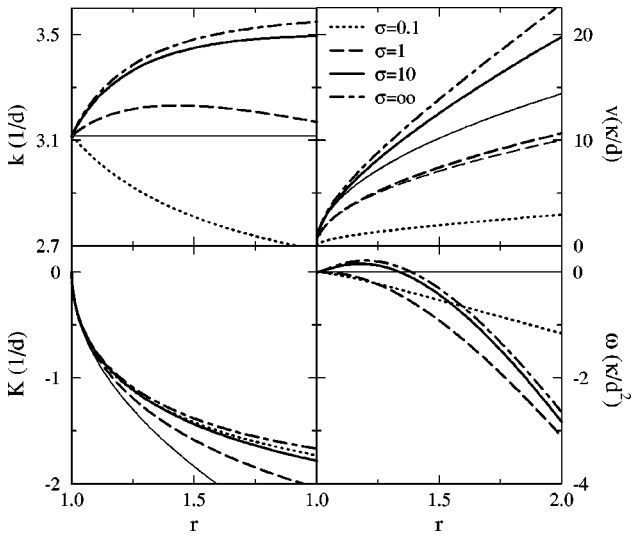

FIG. 4. Comparison of front properties in pure fluids ($\psi=0$) in the absence of throughflow ($Re=0$) resulting from the GLE and from the full field equations. Shown are the selected wave number $k_\pm^*$, velocity $v_-^*=-v_+^*$, spatial growth rate $K_-^*=-K_+^*$, and frequency $\omega_\pm^*$ versus reduced Rayleigh number r for different Prandtl numbers σ as indicated. Thick lines refer to saddle properties of the dispersion of the full field equations obtained with a shooting method. Thin lines refer to the result (5.7) obtained from the GLE.

E. Fronts in mixtures without throughflow

In Fig. 5(a) we compare front properties in a mixture with $\psi=-0.25$ (dashed and full lines) with those in pure fluid convection, $\psi=0$ (dash-dotted lines), both without throughflow. In Fig. 6(a) this comparison is made for $\psi=-0.01$. These results were obtained by evaluating the dispersion $s(Q)$ of the full linear field equations with a many-mode Galerkin expansion (Appendix).

1. Symmetries

Invariance of the field equations under $x\to -x$ for $Re=0$ implies that stationary perturbations with $\omega_c=0$ under a + front are mirror images of those under a − front. This implies for $Re=0$ the symmetry relations

$$(K,\omega,v)_+^{S*} = -(K,\omega,v)_-^{S*};\quad k_+^{S*} = k_-^{S*}. \tag{5.8}$$

This symmetry property of the two front types of S-perturbations with $\omega_c=0$ can be seen in Fig. 5(a) and in Fig. 6(a) for the case $\psi=0$ of pure fluid convection (dashed dotted lines).

Now consider TWD and TWU perturbations. Here the invariance of the field equations (2.12) under $x\to -x$ for $Re=0$ implies first of all that a spatially extended TWD with uniform amplitude is the mirror image of a spatially extended TWU. Furthermore, a TWD under a + front with positive K is symmetry degenerate with a TWU under a −

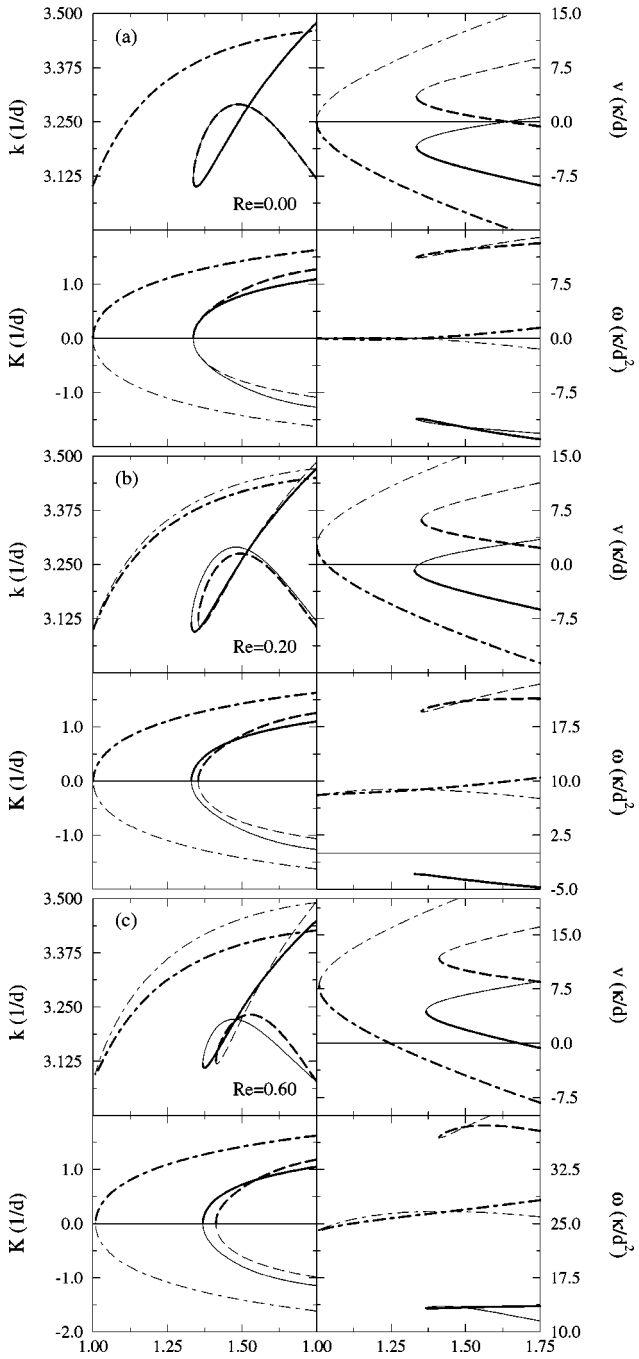

FIG. 5. Front properties in systems with and without throughflow, Re, as indicated. Saddle point results for wave number k^*, velocity v^*, spatial growth rate K^*, and frequency ω^* obtained from the dispersion of the full field equations are shown versus r. Dash-dotted lines refer to fronts in pure fluids ($\psi=0$). Full lines refer to TWU fronts and dashed lines to TWD fronts in mixtures with $\psi=-0.25$. In each case a thick line denotes a $+$ front and a thin line a $-$ front. Parameters are $\sigma=10, L=0.01$.

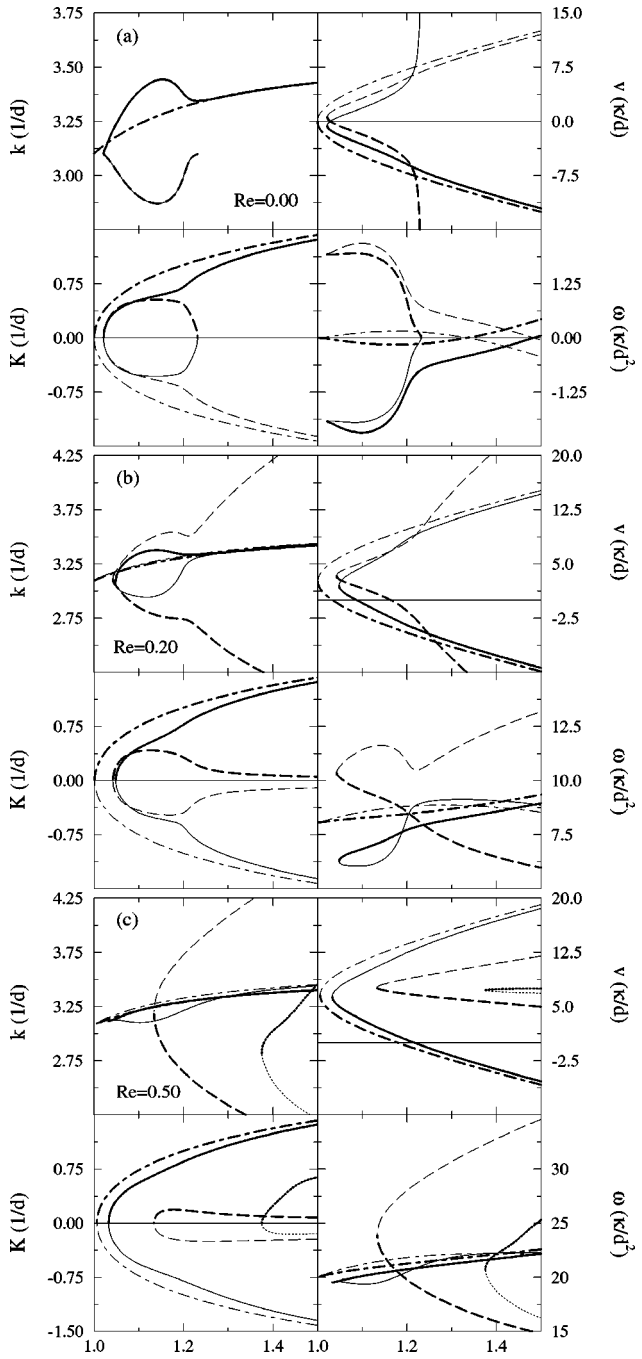

FIG. 6. Front properties in systems with and without throughflow, Re, as indicated. Saddle point results for wave number k^*, velocity v^*, spatial growth rate K^*, and frequency ω^* obtained from the dispersion of the full field equations are shown versus r. Dash-dotted lines refer to fronts in pure fluids ($\psi=0$). Full lines refer to TWU fronts, dashed lines to TWD fronts, and dotted lines in (c) to TWS fronts occurring in mixtures with $\psi=-0.01$. In each case a thick line denotes a $+$ front and a thin line a $-$ front. Parameters are $\sigma=10, L=0.01$.

front with negative K. Similarly a TWU under a $+$ type front is the mirror image of a TWD under a $-$ front (cf. Fig. 3). This implies for $Re=0$ the symmetry relations

$$(K,\omega,v)_{+}^{D*}=-(K,\omega,v)_{-}^{U*}; \quad k_{+}^{D*}=k_{-}^{U*}, \qquad (5.9a)$$

$$(K,\omega,v)_{+}^{U*}=-(K,\omega,v)_{-}^{D*}; \quad k_{+}^{U*}=k_{-}^{D*}. \qquad (5.9b)$$

They can be seen to be realized in Fig. 5(a) and in Fig. 6(a) (cf. dashed and full lines).

The GLE approximation yields beyond Eq. (5.9) additional symmetry relations for $Re=0$ that follow from the fact that, $\tau_0^D=\tau_0^U, \xi_0^D=\xi_0^U$, and $c_1^D=-c_1^U$ [63] for $Re=0$. This then implies according to Eq. (5.6) that within the GLE approximation, for example,

$$K_+^D*=K_+^U*=-K_-^D*=-K_-^U*, \tag{5.10a}$$

$$v_+^D*-v_g^D=v_+^U*-v_g^U \tag{5.10b}$$

holds. Here $v_g^U=-v_g^D$ for $Re=0$.

Inspecting Figs. 5(a) and 6(a) shows, however, that front solutions of the field equations have this additional GLE symmetry (5.10) only close to onset, $r_c^D(Re=0)=r_c^U(Re=0)=r_{osc}$. Further away $K_+^D*\neq K_+^U*$ and $K_-^D*\neq K_-^U*$ so that GLE fronts deviate from those of the full field equations.

2. Dependence on Rayleigh number

For $r=r_{osc}$ the saddle point analysis reproduces the results of the linear stability analysis. The latter yields that at r_{osc} only an extended, spatially uniform plane wave perturbation with the critical wave number can grow. Consequently the saddle point analysis shows that the spatial growth rates of all four fronts vanish, $K_\pm^D*=K_\pm^U*=0$ at r_{osc}. And the front velocities $v_\pm^D*$ and $v_\pm^U*$ start at r_{osc} with the group velocities v_g^D and $v_g^U=-v_g^D$ of the respective critical waves for $Re=0$.

For r values above r_{osc} spatially localized perturbations consisting of wave packets with wave numbers from the unstable band can grow, thus allowing the formation of pulses. The spatial growth rates of their fronts increase with growing r so that the pulses are getting steeper. Also the temporal growth rates increase with growing r. In the top row of Fig. 7 we show the temporal growth rate γ^D (left column) and γ^U (right column) with a combination of contour- and gray-scale plot over the complex Q-plane for $\psi=-0.25$, $Re=0$, and $r=1.65$. At $K=0$, i.e., along the real k-axis one can read off the k-variation of the real parts of the two Hopf eigenvalues $\gamma^D(k)=\gamma^U(k)$ that are symmetry degenerate for $K=0$, $Re=0$. Away from the real k-axis the Hopf bifurcation symmetry for $Re=0$ implies the relation

$$\gamma^D(k,K;r,Re=0)=\gamma^U(k,-K;r,Re=0) \tag{5.11}$$

that is obvious from comparing the top left with the top right plots of Fig. 7. Thus, for $Re=0$ the intersection of the two surfaces of $\gamma^D(Q)$ and $\gamma^U(Q)$ over the complex Q-plane occurs at $K=0$.

The paths of the saddle positions $Q_\pm^D*$ ($Q_\pm^U*$) as a function of r are marked by thick dashed (thick full) lines in the complex Q plane. At r_{osc} all saddles lie on the real k-axis at k_c. Increasing the Rayleigh number above r_{osc} the saddles Q_+^D* and Q_+^U* move towards positive K while Q_-^D* and Q_-^U* move towards negative K. For $r=1.65$ the positions of these four saddles are marked in Fig. 7 by open squares. Since this r-value is close to the border $r_{c-a}^D(Re=0)=r_{c-a}^U(Re=0)$ between convective and absolute instability the temporal growth rates $\gamma_+^D*(Re=0)$ and $\gamma_-^U*(Re=0)$ are

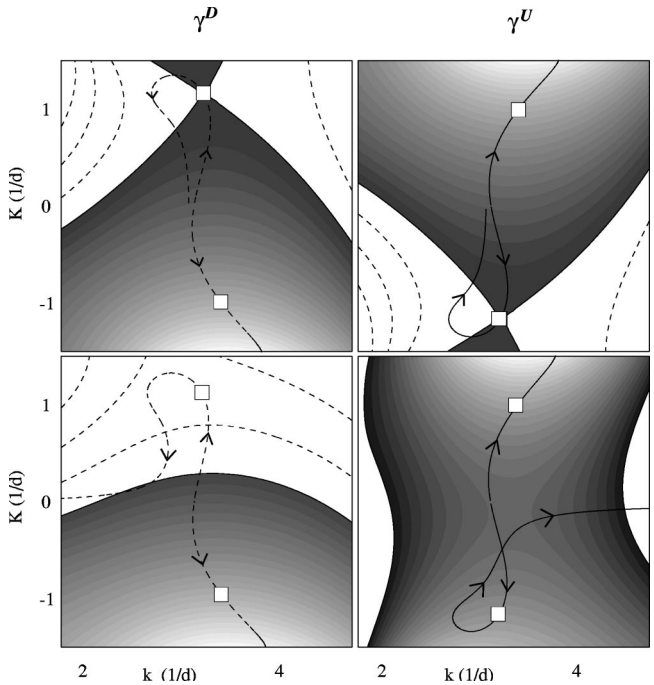

FIG. 7. Temporal growth rates γ^D (left column) and γ^U (right column) for $Re=0$ (top row) and for $Re=0.25$ (bottom row) over the complex Q-plane. Other parameters are $\sigma=10$, $L=0.01$, $\psi=-0.25$, and $r=1.65$. In the white regions with thin dashed γ-isolines γ is negative while $\gamma>0$ in the grey regions. Therein γ decreases with increasing darkness so that the black boundary line between the grey and the white regions is the $\gamma=0$ isoline. The open square in the top (bottom) region of each plot marks the location of the saddle Q_+^* (Q_-^*) for both the D and the U case when $r=1.65$. The dashed (full) lines with arrows in the left (right) column show how the D (U) saddles move as a function of r.

almost zero at the respective saddle positions in the top row of Fig. 7. If one increases r further, then Q_+^D* and Q_-^U* return to the real axis, $K=0$, and vanish there in a collision. This is linked with the fact that for $Re=0$ the TW eigenvalues, $s^D(k,r)$ and $s^U(k,r)$, depending on the real wave number k undergo a transformation from a complex conjugate pair ($\gamma^D=\gamma^U$, $\omega^D=-\omega^U$) to a pair of two distinct real eigenvalues ($\gamma^D\neq\gamma^U$, $\omega^D=-\omega^U=0$) at sufficiently large r [32,40].

The variations of the saddle values of $\gamma*$ and of $K*$ change the front velocities: the velocity of those fronts towards which the phase of the pattern is propagating increases in magnitude while the opposite holds for fronts from which the phase is moving away. This can be seen in Fig. 5(a) and in Fig. 6(a) by comparing v_-^D* (thin dashed line) with v_+^D* (thick dashed line) and $|v_+^U*|$ (thick full line) with $|v_-^U*|$ (thin full line). At the boundary r_{c-a}^D between absolute and convective instability v_+^D* changes sign and a TWD perturbation can spread into the entire system against the group velocity. In the absence of throughflow $r_{c-a}^D=r_{c-a}^U$ so that also v_-^U* changes sign and also the TWU perturbation can expand into the entire system.

Note, that in contradistinction to the GLE result the two fronts of a pulse-like perturbation show also in the absence

of a throughflow different spatiotemporal properties: The spatial growth rate $K_+^{D*}=|K_-^{U*}|$ is bigger than $|K_-^{D*}|=K_+^{U*}$ and the wave numbers $k_+^{D*}=k_-^{U*}$ differ from $k_-^{D*}=k_+^{U*}$. Also the oscillation frequencies $\omega_+^{D*}=-\omega_-^{U*}$ differ from $\omega_-^{D*}=-\omega_+^{U*}$. Therefore our analysis predicts a competition of two different selection processes for convection structures in binary mixtures that grow out of the left and the right front of a pulse-like perturbation being different in wave number, frequency, and spatial envelope profile.

F. Fronts in mixtures with throughflow

The throughflow breaks the symmetry relations that the Hopf bifurcation symmetry imposes for $Re=0$ on the dispersion relations $s^D(Q)$ and $s^U(Q)$ of TWD and TWU perturbations, respectively. Hence the symmetry relations (5.9) between the saddle properties for $Re=0$ and the ensuing relations between properties of TWD fronts and of TWU fronts do not longer hold for $Re>0$. However, the influence of a finite throughflow on the front properties can be understood to a large extent on the basis of the GLE prediction for the throughflow-induced changes. Therefore, we first review the latter briefly.

The Re dependence of the coefficients in the GLE for TWD and TWU perturbations [61] shows that the frequencies $\omega_c^{D,U}$ and the group velocities $v_g^{D,U}$ are changed most by a small throughflow. These quantities increase linearly for small Re,

$$\omega_c^{D,U}(Re)=\pm\omega_H+aRe,$$
$$v_g^{D,U}(Re)=\pm v_g^0+bRe, \tag{5.12a}$$

with ω_H, v_g^0, a, and b all being positive. This behavior together with the GLE result (5.6) for the front velocities v^* and the front frequencies ω^* explains much of the upwards shift of v^* and ω^*, respectively, that results from the field equations when the throughflow is switched on: A comparison of the plots in Figs. 5 and 6 for ω^* and v^* at $Re=0$ in (a) with the plots at $Re>0$ in (b) and (c) shows that the throughflow shifts the front velocities v^* and the phase velocities ω^*/k^* upwards towards more positive values.

Compared to the large throughflow-induced changes in ω_c, ω^*, v_g, and v^* the changes predicted by the GLE approximation (5.6) for k^* and K^* are relatively small coming only from the small variations of ξ_0, k_c, and c_1 with Re. Thus, in Figs. 5 and 6 also the front values of k^* and K^* obtained for the full field equations do not change much when switching on the throughflow while, however, the topology of the curves of the front properties versus r changes somewhat.

Since the throughflow breaks the symmetry relations (5.9) holding for $Re=0$ one finds, e.g., that wave numbers and intensity profiles of a D_+ front and of a U_- front differ when $Re>0$. This holds in particular also for the vicinity of the bifurcation thresholds $r_c^U(Re)\neq r_c^D(Re)$ for TWU and TWD patterns, respectively, that are located at different intersections of the respective K^*-curves with the r-axis. They mark fronts with spatial growth rates $K^*\to 0$ that become possible right at the bifurcation thresholds r_c^U and r_c^D with critical onset wave numbers k_c^U and k_c^D, respectively. The critical thresholds and wave numbers are for TWU and TWD patterns different when $Re>0$ while they are symmetry degenerate for $Re=0$.

Besides that and in addition to it one has above the respective thresholds that, e.g., $K_+^{D*}\neq -K_-^{D*}$ and $K_+^{U*}\neq -K_-^{U*}$. Hence the two fronts of a TWD or of a TWU pulselike perturbation are different. This difference occurs, however, already in the absence of throughflow (cf. the discussion at the end of Sec. V E 2).

To understand the variation of the growth rates $\gamma^{D,U}(k,K;Re)$ over the complex Q-plane and its change with increasing Re (bottom row in Fig. 7) one can again invoke the GLE approximation (4.11) for the dispersion. It yields

$$\gamma=-v_gK+\frac{\mu}{\tau_0}-\frac{\xi_0^2}{\tau_0}[(k-k_c)^2-K^2+2c_1(k-k_c)K]. \tag{5.13}$$

Now $\tau_0^{D,U}(Re)$, $\xi_0^{D,U}(Re)$, and $c_1^{D,U}(Re)$ do not deviate much from their respective $Re=0$ values whereas $v_g^{D,U}(Re)=\pm v_g^0+bRe$ varies linearly in Re as noted in Eq. (5.12a). Thus, the throughflow tilts the $Re=0$ surfaces of $\gamma^{D,U}$ over the Q-plane by the common term $\propto -ReK$ such as to increase (decrease) γ for negative (positive) K. This leads for the parameters of Fig. 7 to an almost symmetric variation of γ^U with K around $K=0$ while γ^D becomes negative for almost all positive K and the intersection line where $\gamma^D(Q)=\gamma^U(Q)$ is no longer located at the real axis $K=0$. Also the saddle positions change. In particular K_+^{D*} and K_-^{U*} do no longer merge at larger r with the real Q axis above onset of convection (cf. bottom row of Fig. 7).

The influence of the Soret coupling strength on the saddle points can be seen by comparing the results for $\psi=-0.25$ in Fig. 5 with those for $\psi=-0.01$ in Fig. 6. In the absence of throughflow, $Re=0$, one observes in Fig. 6(a) for $\psi=-0.01$ at $r\approx 1.21$ the transition $(K,\omega)_+^{D*}=-(K,\omega)_-^{U*}\to 0$ of a complex conjugate pair of eigenvalues to two distinct real eigenvalues [32,40] that was mentioned already in Sec. V E 2. There the D_+ saddle and the U_- saddle collide and disappear [40] yielding a formal divergence of v. Any finite throughflow lifts the symmetry degeneration and prevents this saddle collision with the associated transition to real eigenvalues. Then the D_+ and the U_- saddles do not end on the real k-axis but keep moving separately with increasing r.

However, between $Re=0$ and $Re=0.2$ [Figs. 6(a) and 6(b), respectively] there does occur a collision of the D_- and the U_- saddles at negative K after which the identification of these saddles becomes interchanged [40]. Thus in Fig. 6(a) the thin *full* lines identifying the U_- saddle properties approach for large r the properties of the $-$ saddle in pure fluids (thin dash-dotted lines). Whereas in Fig. 6(b) it is the D_- saddle properties (thin *dashed* lines) that approach for large r the pure fluid limiting behavior. These saddle collision properties are somewhat involved [40] and will therefore not be discussed further here. We also mention only

briefly that at large Re in Fig. 6(c) there appear the TWS saddles (dotted lines). They have moved with increasing Re first downwards in r thereby approaching the TWD saddles. Then, upon increasing Re further the TWD and TWS saddles move—after an interval with more complex behavior [40]—upwards in r and thus lose their experimental relevance.

For strong throughflow rates the TWU saddle properties (full lines in Figs. 5 and 6) approach at large r those of pure fluid convection (dashed-dotted lines in Figs. 5 and 6). This is especially visible for the smaller Soret coupling strength $\psi=-0.01$. It reflects the physical property that with increasing throughflow and with increasing heating not only the nonlinear behavior of well mixed binary fluids [18] but also the linear properties of perturbations [32] become more and more similar to those of pure fluids. For stronger Soret coupling this happens at larger and larger Re, r.

VI. SIMULATIONS OF THE NONLINEAR FIELD EQUATIONS

In order to check and to compare the spatiotemporal properties of fronts and pulses that were obtained in the previous section from the saddle point analysis of the dispersion relation of the *linear* field equations we present here some representative results that were obtained from a numerical solution of the full *nonlinear* hydrodynamical field equations.

A. System

In order to study the structural dynamics of fronts and pulses we performed numerical simulations of convection in a long and narrow rectangular convection channel of length $\Gamma=80$ in x-direction. To that end we used a finite-difference code (Appendix) to solve the time dependent nonlinear field equations (2.1). In such channels that are narrow in y-direction convection occurs in the form of straight parallel rolls with axes aligned in y-direction. The field variations in y-direction may be ignored for our purposes since these convection structures are effectively 2D so that a description in the $x-z$ midplane perpendicular to the roll axes suffices.

In our simulations the channel was closed at $x=0$ and $x=\Gamma$ by rigid impermeable lateral sidewalls, each of which had a thickness of 2. However, when simulating convection in the presence of throughflow we imposed the plane horizontal Poiseuille profile $U(z)$ (2.10) as a boundary condition at $x=0$ and $x=\Gamma$. The ratio of the heat diffusivities of the sidewalls κ_w and of the binary fluid κ was chosen to be $\kappa_w/\kappa=0.43$ and $\Lambda_w/\Lambda=1.23$ was the ratio of the respective heat conductivities. Thus we solved the diffusion equation

$$\partial_t T_w=\kappa_w(\partial_x^2+\partial_z^2)T_w \tag{6.1}$$

for the temperature T_w in the sidewalls subject to the boundary conditions

$$T_w=T \quad \text{and} \quad \partial_x T_w=\frac{\Lambda}{\Lambda_w}\partial_x T \quad \text{at} \quad x=0, \quad \Gamma, \tag{6.2a}$$

$$\partial_x T_w=0 \quad \text{at} \quad x=-2, \quad \Gamma+2. \tag{6.2b}$$

Hence the temperature and the lateral heat current vary continuously at the inner sidewall surface so that convective temperature variations generated in the fluid penetrate to some extent the sidewalls. At the outside surface of the sidewalls we imposed the lateral heat flux to vanish.

B. Results

The simulations discussed here were done for fluid parameters $\sigma=10$, $L=0.01$, and $\psi=-0.25$. Each run was started from a spatially localized initial perturbation in the temperature field that was perfectly symmetric around the middle of the cell. The center of gravity of the initial perturbation of the homogeneous conductive state was exactly at $x=40$. The resulting evolution of the lateral profiles of the temperature field at midheight, $z=0$, of the cell is shown with so-called hidden line plots for different supercritical Rayleigh numbers in Figs. 8 and 9 for $Re=0$ and $Re=0.05$, respectively.

1. Absence of throughflow

The above described symmetric initial perturbation generates in the absence of throughflow, $Re=0$, two pulses shown in Fig. 8 that are mirror images of each other. The left (right) one consists of TWU (TWD) perturbations whose phase is propagating to the left (right). If the initial perturbation is not mirror symmetric but of some arbitrary generic, albeit localized form then it still generates TWU and TWD pulses. However, their amplitudes are generically different depending on the magnitude of the overlap of the initial perturbation with the critical TWU and TWD eigenfunctions, respectively. Only in the nongeneric case of an initial perturbation being a pure wave packet in the sense that it consists of TWU or TWD excitations only can one observe the growth of only one pulse, TWU or TWD [66].

In the top part of Fig. 8 we show the pulse evolution between $t=0$ and $t=10$ for $r=1.341$ which is very close to the oscillatory bifurcation threshold r_{osc} for $\psi=-0.25$. The group velocities of the TW perturbations in Fig. 8 are in the same directions as the respective phase velocities. Thus the TWU (TWD) pulse moves to the left (right). Because of the vicinity to the Hopf threshold the phase velocities of the waves and the group velocities of the pulses are large and the wave amplitudes grow exponentially in time. Furthermore, the pulse shape remains almost Gaussian as the imposed initial perturbation. The latter is shown in the lowest profile in the top part of Fig. 8.

A perfectly symmetric Gaussian behavior around the respective pulse center would result from the GLE approximation. Therein the spatial growth rates of all four fronts would be the same. Also the front velocities relative to the velocities of the two pulse centers, $v_g^U=-v_g^D$, would be the same according to (5.6), (5.10). While the pulse centers separate in the top part of Fig. 8 with twice the group velocity of TWD or TWU perturbations the velocities of the four fronts are not the same. They agree, however, very well with the results, $v_+^{D*}=-v_-^{U*}=2.97$ and $v_-^{D*}=-v_+^{U*}=3.93$, that we obtained from the saddle point analysis of the linear field equations and that are displayed in Fig. 5(a) (with the line con-

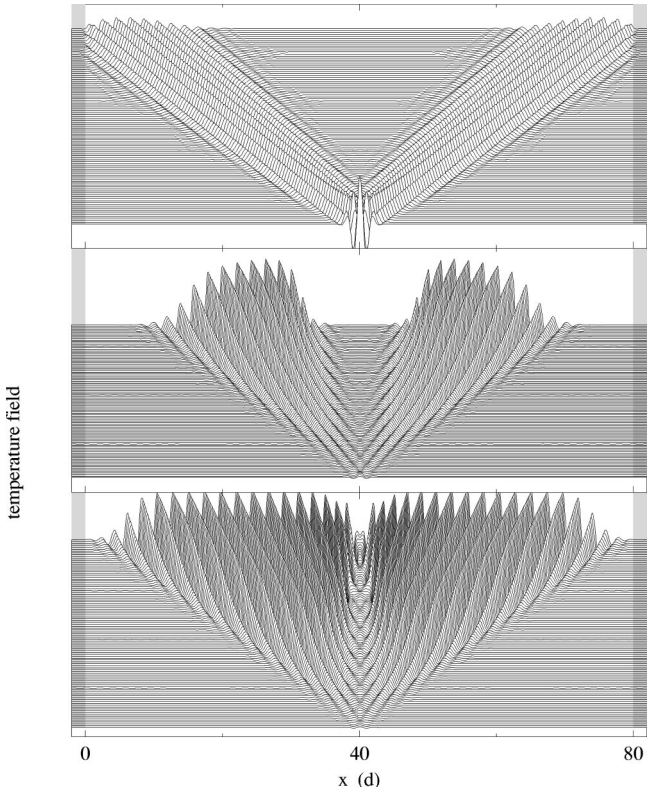

FIG. 8. Direct numerical simulation of convection pulses originating in the absence of throughflow from a symmetrical localized initial perturbation. Shown are hidden-line plots of equidistantly spaced snapshots, staggered one above the other, of the lateral variation of the temperature at midheight, $z=0$. They cover intervals of length 10 ($r=1.342$, top part), 5 ($r=1.518$, middle part), and 5 thermal diffusion times ($r=1.671$, bottom part), respectively. Parameters are $\sigma=10$, $L=0.01$, $\psi=-0.25$, and $Re=0$. Grey vertical stripes locate thermally conducting sidewalls that close the convection cell laterally (cf. text for details).

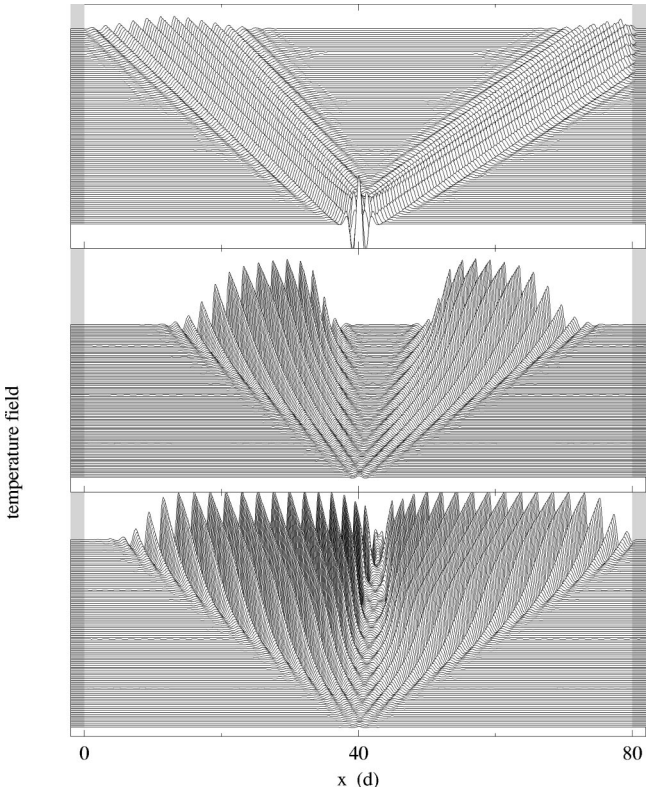

FIG. 9. Direct numerical simulation of convection pulses originating in the presence of a small throughflow from a symmetrical localized initial perturbation. Shown are hidden-line plots of equidistantly spaced snapshots, staggered one above the other, of the lateral variation of the temperature at midheight, $z=0$. They cover intervals of length 10 ($r=1.342$, top part), 5 ($r=1.518$, middle part), and 5 thermal diffusion times ($r=1.671$, bottom part), respectively. Parameters are $\sigma=10$, $L=0.01$, $\psi=-0.25$, and $Re=0.05$. Grey vertical stripes locate thermally conducting sidewalls that close the convection cell laterally (cf. text for details).

vention D: dashed, U: full, $+$: thick, and $-$: thin). Note that the four fronts of the two pulses in Fig. 8 obey the mirror symmetry relations (5.9) in the absence of throughflow between the two trailing fronts, D_+ and U_-, and between the two leading fronts, D_- and U_+, respectively. Here trailing and leading refers to the direction of phase propagation of the underlying waves.

With the Rayleigh number so close to the Hopf bifurcation the conductive state of the top part of Fig. 8 is only convectively unstable (cf. lower right corner of Fig. 1). Therefore both, the $+$ as well as the $-$ front of each pulse, move into the same direction as the pulse center. Hence, behind the two trailing convection fronts, D_+ and U_-, the system returns to the basic conductive state and the region between these fronts with quiescent fluid in the center of the cell grows. In a finite cell, however, the pulses are reflected off the sidewalls [14] and propagate inwards with some reduced amplitude [11,12,40]. For the setup of the top part of Fig. 8 the fronts had reached the sidewalls at about 10 vertical thermal diffusion times.

If one increases the Rayleigh number to $r=1.518$ (middle part of Fig. 8) which is shortly below the border between convective and absolute instability (triangle in the lower right corner of Fig. 1 at $Re=0$) then the trailing D_+ and U_- fronts that are oriented towards the center of the cell move much slower, their front velocities are reduced to $v_+^{D*}=-v_-^{U*}=0.77$. The velocities of the two leading fronts, D_- and U_+, have increased to $v_-^{D*}=-v_+^{U*}=6.62$ [cf. also Fig. 5(a)]. Therefore we show in the middle part of Fig. 8 only the time interval from $t=0$ to $t=5$ to avoid front collisions with the walls.

The asymmetry of the pulse shapes that is predicted by the saddle point analysis is reproduced by our nonlinear numerical simulations: the trailing fronts with spatial growth rates $K_+^{D*}=-K_-^{U*}=0.95$ have become significantly steeper than the leading fronts with $K_-^{D*}=-K_+^{U*}=-0.83$, cf. Fig. 5(a). Also the wave amplitudes increase there more rapidly in time.

During an initial period in time one can see in the middle part of Fig. 8 a transient behavior where TWD and TWU perturbations are superimposed to form a standing wave under the two overlapping trailing fronts before they fully separate. Such behavior can also be seen for a longer time in the bottom part of Fig. 8. There the Rayleigh number has been

increased to $r=1.671$. Here the leading front velocities have increased to $v_-^{D*}=-v_+^{U*}=8.08$ [cf. also Fig. 5(a)]. But, more importantly, the trailing D_+ and U_- fronts that are oriented towards the center of the cell have reversed their propagation direction. According to the saddle point analysis one has here $v_+^{D*}=-v_-^{U*}=-0.24$, cf. Fig. 5(a), so that one has entered here the absolute instability range of the conductive state, cf. Fig. 1, where the two fronts of a pulse move in opposite direction.

Thus, the TWD state in the right part of the cell would expand also to the left and the TWU in the left part of the cell would expand also to the right if these fronts were free to move into quiescent fluid. Instead, these two counterpropagating D_+ and U_- fronts collide and thereby they first generate a longer lasting initial transient with standing waves than at the smaller r in the middle part of Fig. 8. However, the time interval during which TWD and TWU perturbations combine linearly to a standing wave is restricted by the growth of nonlinear interactions between TWD and TWU that become relevant when their amplitudes have grown sufficiently. They cause a destructive interference of the two colliding fronts in the center region thereby creating a source defect. This defect connection between the developed TWU and TWD patterns with left moving phase in the left part of the cell and right moving phase in the right part of the cell is stable and stationary for our perfectly symmetric setup and initial conditions. Source and sink defects have been investigated experimentally by Kolodner [65] and Kaplan and Steinberg [46,64].

2. Finite throughflow

A finite throughflow breaks the mirror symmetry between TWD and TWU pulses as can be seen in Fig. 9 for the small throughflow $Re=0.05$. The respective three parts of Fig. 8 and of Fig. 9 refer to the same Rayleigh numbers so that one can immediately see the effect of the throughflow on the spatiotemporal evolution of localized perturbations. First of all it shifts all velocities of convective perturbations upwards to more positive values. This holds for the velocities of the centers of the two pulses in Fig. 9 as well as for the velocities of the two fronts of each pulse. For example, the leading D_- front of the right TWD pulse is now moving faster downstream to the outlet at $x=\Gamma$ than without throughflow and faster than the leading U_+ front of the left TWU pulse is moving upstream towards the inlet, $x=0$.

Also the velocities v_+^{D*} and v_-^{U*} of the trailing D_+ and U_- fronts, respectively, are now different. Hence the borders r_{c-a}^D and r_{c-a}^U between convective and absolute instability against TWD and TWU perturbations where v_+^{D*} and v_-^{U*}, respectively, change sign are now different (cf. downwards and upwards pointing triangles in Fig. 1). In the top part of Fig. 9 the conductive state is well within the range of convective instability (Fig. 1) against TWD as well as TWU perturbations with both fronts of each pulse moving into the same direction. In the middle part of Fig. 9 at $r=1.518$, however, where v_-^{U*} is almost zero the TWU perturbations of the left pulse are about to expand also in downstream direction — the boundary r_{c-a}^U (upwards pointing triangles in the lower right corner of Fig. 1) decreases upon switching on the throughflow. On the other hand, the TWD perturbations are more easily blown out of the system — the boundary r_{c-a}^D (downwards pointing triangles in the lower right corner of Fig. 1) increases with Re and so does v_+^{D*}.

As an aside we mention here that one can at a sufficiently large Re (of about 0.5 according to Fig. 1) enter again the convectively unstable range by crossing the right part of the r_{c-a}^U curve when the throughflow becomes so large that the leading U_+ front of the left TWU pulse reverts its motion into downstream direction — then the TWU pulse moves out of the system; this time however in downstream direction.

At $r=1.671$ and $Re=0.05$ in the lower part of Fig. 9 the boundary r_{c-a}^D (downwards pointing triangles in the lower right corner of Fig. 1) has just been crossed, the conductive state is absolutely unstable both against TWD as well as against TWU perturbations, the front velocities v_+^{D*} and v_-^{U*} have changed their signs, and consequently the D_+ front and the U_- front collide thereby creating a source defect in the center of the cell. Now, however, with $Re>0$ this defect moves downstream with the throughflow.

Finally we would like to stress that the analysis presented here refers to the spatiotemporal growth behavior of *small* TW perturbations of the conductive state only. The analysis of the bifurcation properties of spatially extended, nonlinearly saturated TW solutions shows, for example, that for sufficiently large throughflow stable nonlinear TWU states are not available for linear TWU perturbations to grow to. Then, a nonlinear transformation from an intermediate TWU to a final saturated TWD state occurs that is accompanied by a somewhat spectacular reversal of the phase propagation [67].

VII. CONCLUSION

Spatiotemporal properties of spatially localized structures have been analyzed that consist of convective perturbations of the basic conductive state of a horizontal binary fluid layer heated from below and the effect of a plane horizontal Poiseuille flow on them has been determined. To that end the behavior of linear fronts and of pulse-like wave packets formed out of the three different perturbations — two oscillatory ones and a stationary one — that are relevant in binary mixture convection has been investigated. This was done by analyzing the appropriate saddle points of the complex dispersion relations $s(Q)$. The latter are obtained numerically as functions of the complex wave number $Q=k-iK$ from the full linearized field equations for the three different perturbations in question. We also determined these functions within a Ginzburg-Landau amplitude equation approximation to compare with its predictions for the front and pulse behavior in pure fluids ($\psi=0$) and in mixtures ($\psi\neq 0$) as a function of the throughflow.

We first briefly reviewed the linear bifurcation properties of different spatially *extended* convective patterns that have spatially homogeneous amplitudes and how they are influenced by a lateral throughflow thereby providing the background and the frame for discussing our findings on the behavior of spatially *localized* perturbations. The results of this

earlier study that are most important for understanding the behavior of spatially *localized* perturbations are that the symmetry degeneracy of the Hopf bifurcation of the conductive state at r_{osc} into two left or right propagating TW's with frequencies $\pm\omega_H$ is broken: In the presence of a throughflow the dispersion relations, $s^U(Q)$ and $s^D(Q)$, and thus the bifurcation thresholds and the spatiotemporal behavior of the upstream traveling wave (TWU) and of the downstream traveling wave (TWD) are different. Furthermore, in mixtures with negative Soret coupling the bifurcation threshold $r_c^S(Re)$ for TWS structures, which become a stationary pattern when $Re=0$ but propagate when $Re>0$, gets strongly depressed by a small throughflow. These findings allow to understand also to a large extent the variation of the transition boundaries between the parameter regions in which the conductive state is convectively or absolutely unstable against TWD, TWU, or TWS perturbations, repectively.

We have determined these boundaries where one of the fronts of a pulse-like wave packet reverts its propagation direction in the laboratory frame by a saddle point analysis of the respective dispersion relations $s^D(Q)$, $s^U(Q)$, and $s^S(Q)$ as functions of Re for different Soret coupling strengths. Furthermore and in addition to it we have determined the general front behavior of TWD, TWU, and TWS patterns each under an intensity envelope with a spatial variation of type $+$ (growth in positive x-direction) or an envelope with a spatial variation of type $-$ (growth in negative x-direction). Our interest was focused on small Reynolds numbers since for large Re the externally imposed shear flow effectively eliminates the Soret-induced coupling effects between the convective concentration field and the other fields by suppressing vertical convective transport of Soret driven concentration perturbations.

The combination of the three different dynamics of the constituent perturbations (TWD, TWU, TWS) and the two different spatial profiles $(+,-)$ leads to six different fronts of the form $f(x,t)\sim e^{i(k^*x-\omega^*t)}e^{K^*(x-v^*t)}$ in laboratory space. Their velocity v^*, spatial growth rate K^*, wave number k^*, and frequency ω^* as determined via a saddle point analysis of the respective dispersion relations differ in general from each other in the presence of a throughflow. For $Re=0$, however, the invariance of the field equations under $x\to -x$ implies symmetry relations like, e.g., stationary perturbations with $\omega_c=0$ under a $+$ front are mirror images of those under a $-$ front, a TWD under a $+$ front with positive K is symmetry degenerate with a TWU under a $-$ front with negative K, and a TWU under a $+$ type front is the mirror image of a TWD under a $-$ front. However, the two fronts of a pulse-like perturbation show also in the absence of a throughflow different spatiotemporal properties: The spatial growth rate $K_+^{D*}=|K_-^{U*}|$ is bigger than $|K_-^{D*}|=K_+^{U*}$ and the wave numbers $k_+^{D*}=k_-^{U*}$ differ from $k_-^{D*}=k_+^{U*}$. Also the oscillation frequencies $\omega_+^{D*}=-\omega_-^{U*}$ differ from $\omega_-^{D*}=-\omega_+^{U*}$ and the velocity of those fronts (D_-,U_+) towards which the phase of the pattern is propagating grows with increasing Rayleigh number while the opposite holds for the fronts (D_+,U_-) from which the phase is moving away. Hence our analysis predicts a competition of two different selection processes for convection structures in binary mixtures that grow out of the left and the right front of a pulse-like perturbation being different in wave number, frequency, and spatial envelope profile.

A finite throughflow breaks the relations that the Hopf bifurcation symmetry imposes for $Re=0$ on the dispersion relations $s^D(Q)$ and $s^U(Q)$ of TWD and TWU perturbations, respectively. Hence the symmetry relations between the saddle properties for $Re=0$ and the ensuing relations between properties of TWD fronts and of TWU fronts no longer hold for $Re>0$. In particular there is an overall throughflow induced upwards shift of front velocities v^* and of phase velocities ω^*/k^* towards more positive values.

Finally we compared the spatiotemporal properties of fronts that were obtained from the saddle point analysis of the dispersion relation of the *linear* field equations with numerical solutions of the full *nonlinear* hydrodynamical field equations. To that end we simulated pulses not only in the convectively unstable parameter regimes, where both, the $+$ and the $-$ front propagate (with different front velocities) into the same direction as the pulse center, but also in the absolutely unstable regime where the two fronts of the pulse move into opposite directions. These results agree for $Re=0$ as well as for finite Re with the spatiotemporal properties of fronts obtained from the saddle point analysis.

ACKNOWLEDGMENT

This work was supported by the Deutsche Forschungsgemeinschaft.

APPENDIX: NUMERICAL METHODS

To determine the dispersion relations $s(Q)$ of the linear field equations, i.e., the three eigenvalues s^S, s^U, and s^D of the eigenvalue problem (2.18) as functions of the complex wave number $Q=k-iK$ we used a shooting method that is described in Ref. [32] and/or a Galerkin method. Therein we expanded the complex z dependent eigenfunctions $\hat{\Phi}=(\hat{w},\hat{\theta},\hat{\zeta})$ that have positive parity under $z\to -z$ as follows:

$$\hat{w}(z)=\sum_{n=1}\hat{w}_n C_n(z), \tag{A1a}$$

$$\hat{\theta}(z)=\sum_{n=0}\hat{\theta}_n\sqrt{2}\cos[(2n+1)\pi z], \tag{A1b}$$

$$\hat{\zeta}(z)=\sum_{n=0}\hat{\zeta}_n\sqrt{2-\delta_{n,0}}\cos(2n\pi z). \tag{A1c}$$

Here $C_n(z)$ are Chandrasekhar functions [68]. Inserting Eq. (A1) into Eq. (2.18) yields after projection onto the normal modes an algebraic system of equations for the complex mode amplitudes $\hat{w}_n,\hat{\theta}_n$, and $\hat{\zeta}_n$. The solvability condition $\mathcal{D}(\sigma,L,\psi,Re,r,Q,s)=0$ that requires the determinant $\mathcal{D}$ of this system of equations to vanish yields the three dispersion relations as the roots of $\mathcal{D}=0$.

In particular in the presence of a finite throughflow we found the Galerkin method to be significantly faster and more robust than the shooting method. The advantages of the former are that it does not require explicit integrations, say of Runge-Kutta type, and that the solvability condition $\mathcal{D}(\sigma,L,\psi,Re,r,Q,s)=0$ can be written in terms of analytical expressions.

For the sake of comparison and crosscheck we also integrated the *nonlinear* field equations (2.1) using a modification of the SOLA code that is based on the MAC method [69,70]. This is a finite-difference method of second order in space formulated on staggered grids for the different fields with a uniform spatial resolution for which we took $\Delta x = \Delta z = 0.025$. An explicit first-order Euler step in time was used in the balance equations of heat (2.1b) and concentration (2.1c) and a second order DuFort-Frankel-scheme in time was used in the momentum balance equation (2.1d). The Poisson equation for the pressure field that results from taking the divergence of Eq. (2.1d) was solved iteratively using the artificial viscosity method [70].

[1] M. C. Cross and P. C. Hohenberg, Rev. Mod. Phys. **65**, 851 (1993).

[2] J. K. Platten and J. C. Legros, *Convection in Liquids* (Springer-Verlag, Berlin, 1984).

[3] M. C. Cross and K. Kim, Phys. Rev. A **37**, 3909 (1988); *ibid.* **38**, 529 (1988).

[4] E. Knobloch and D. R. Moore, Phys. Rev. A **37**, 860 (1988).

[5] W. Hort, Diploma thesis, Saarbrücken, 1990.

[6] P. Kolodner, A. Passner, C. M. Surko, and R. W. Walden, Phys. Rev. Lett. **56**, 2621 (1986).

[7] C. M. Surko and P. Kolodner, Phys. Rev. Lett. **58**, 2055 (1987).

[8] V. Steinberg and E. Kaplan, in *Spontaneous Formation of Space-Time Structures and Criticality*, edited by T. Riste and D. Sherrington (Kluwer Academic, Amsterdam, 1991), p. 207 contains a review on counterpropagating wave and blinking state convection in rectangular containers.

[9] P. Kolodner, C. M. Surko, and H. Williams, Physica D **37**, 319 (1989).

[10] J. Fineberg, E. Moses, and V. Steinberg, Phys. Rev. Lett. **61**, 838 (1988); P. Kolodner, *ibid.* **63**, 578 (1989); J. Fineberg, E. Moses, and V. Steinberg, *ibid.* **63**, 579 (1989).

[11] M. C. Cross, Phys. Rev. A **38**, 3593 (1988).

[12] J. Fineberg, V. Steinberg, and P. Kolodner, Phys. Rev. A **41**, 5743 (1990).

[13] P. Kolodner, C. M. Surko, H. L. Williams, and A. Passner, in *Propagation in Systems Far From Equilibrium*, edited by J. E. Wesfreid, H. R. Brand, P. Manneville, G. Albinet, and N. Boccara (Springer-Verlag, Berlin, 1987), p. 282.

[14] P. Kolodner, C. M. Surko, A. Passner, and H. L. Williams, Phys. Rev. A **36**, 2499 (1987).

[15] P. Kolodner and J. A. Glazier, Phys. Rev. A **42**, 7504 (1990).

[16] For a review see [2,1]. Further references may be found, e.g., in [17,18]. See also the more recent publications [19–25] of some of the many groups that have investigated convection in binary mixtures.

[17] W. Barten, M. Lücke, M. Kamps, and R. Schmitz, Phys. Rev. E **51**, 5636 (1995); **51**, 5662 (1995).

[18] M. Lücke, W. Barten, P. Büchel, C. Fütterer, S. Hollinger, and Ch. Jung, in *Evolution of Structures in Dissipative Continous Systems*, edited by F. H. Busse and S. C. Müller, Lecture Notes in Physics, **m55** (Springer-Verlag, Berlin, 1998), p. 127.

[19] E. Kaplan, E. Kuznetsov, and V. Steinberg, Phys. Rev. E **50**, 3712 (1994).

[20] P. Kolodner, Phys. Rev. E **50**, 2731 (1994).

[21] H. Touiri, J. K. Platten, and G. Chavepeyer, Eur. J. Mech. B/Fluids **15**, 241 (1996).

[22] L. Ning, Y. Harada, and H. Yahata, Prog. Theor. Phys. **97**, 83 (1997).

[23] A. Spina, J. Toomre, and E. Knobloch, Phys. Rev. E **57**, 524 (1998).

[24] A. La Porta and C. M. Surko, Physica D **23**, 21 (1998).

[25] K. Lerman, D. S. Cannell, and G. Ahlers, Phys. Rev. E **59**, 2975 (1999).

[26] P. Kolodner, J. A. Glazier, and H. Williams, Phys. Rev. Lett. **65**, 1579 (1990).

[27] L. D. Landau and E. M. Lifshitz, *Fluid Mechanics* (Pergamon, Oxford, 1959).

[28] P. Kolodner, H. L. Williams, and C. Moe, J. Chem. Phys. **88**, 6512 (1988).

[29] W. Hort, S. J. Linz, and M. Lücke, Phys. Rev. A **45**, 3737 (1992).

[30] J. Liu and G. Ahlers, Phys. Rev. E **55**, 6950 (1997).

[31] H. B. Squire, Proc. R. Soc. London, Ser. A **142**, 621 (1933).

[32] Ch. Jung, M. Lücke, and P. Büchel, Phys. Rev. E **54**, 1510 (1996). JLB scale temperatures by $\kappa\nu/(\alpha g d^3)$ and concentration by $\kappa\nu/(\beta g d^3)$. Thus the relation between the respective reduced fields is $T_{JLB}=RaT$ and $C_{JLB}=RaC$.

[33] W. Schöpf and W. Zimmermann, Phys. Rev. E **47**, 1739 (1993).

[34] G. W. T. Lee, P. Lucas, and A. Tyler, J. Fluid Mech. **135**, 235 (1983).

[35] S. Hollinger and M. Lücke, Phys. Rev. E **52**, 642 (1995).

[36] S. J. Linz and M. Lücke, Phys. Rev. A **35**, 3997 (1987); in *Propagation In Systems Far From Equilibrium*, edited by J. E. Wesfreid, H. R. Brand, P. Manneville, G. Albinet, and N. Boccara (Springer-Verlag, Berlin, 1988), p. 292.

[37] D. T. J. Hurle and E. Jakeman, J. Fluid Mech. **47**, 667 (1971).

[38] T. Clune and E. Knobloch, Physica D **61**, 106 (1992).

[39] H. W. Müller, M. Lücke, and M. Kamps, Europhys. Lett. **10**, 451 (1989); Phys. Rev. A **45**, 3714 (1992).

[40] P. Büchel, Ph.D. thesis, Universität des Saarlandes, Saarbrücken, 1999.

[41] K. Lerman, E. Bodenschatz, D. S. Cannell, and G. Ahlers, Phys. Rev. Lett. **70**, 3572 (1993).

[42] A. La Porta, K. D. Eaton, and C. M. Surko, Phys. Rev. E **53**, 570 (1996); A. La Porta and C. M. Surko, *ibid.* **53**, 5916 (1996); **56**, 5351 (1997); **55**, R6327 (1997).

[43] K. Lerman, G. Ahlers, and D. S. Cannell, Phys. Rev. E **53**, R2041 (1996).

[44] H. W. Müller, M. Tveitereid, and S. Trainoff, Phys. Rev. E **48**, 263 (1993).
[45] M. Dressler, Diploma thesis, Universität des Saarlandes, Saarbrücken, 1995.
[46] E. Kaplan and V. Steinberg, Phys. Rev. E **48**, R661 (1993).
[47] V. Steinberg, J. Fineberg, E. Moses, and I. Rehberg, Physica D **37**, 359 (1989).
[48] J. Fineberg, E. Moses, and V. Steinberg, Phys. Rev. A **38**, 4939 (1988).
[49] E. Moses, J. Fineberg, and V. Steinberg, Phys. Rev. A **35**, 2757 (1987).
[50] R. J. Briggs, *Electron-Stream Interaction with Plasmas*, Research Monograph No. 29 (M.I.T. Press, Cambridge, MA, 1964); A. Bers, *Linear Waves and Instabilities* (Physique des Plasmas, New York, 1975).
[51] P. Huerre, in *Instabilities and Nonequilibrium Structures*, edited by E. Tirapegui and D. Villaroel (Reidel, Holland, 1987), p. 141.
[52] W. van Saarloos and P. C. Hohenberg, Physica D **56**, 303 (1992); **69**, 209(E) (1993).
[53] J. M. Chomaz, Phys. Rev. Lett. **69**, 1931 (1992); A. Couairon and J. M. Chomaz, Physica D **108**, 236 (1997)
[54] R. J. Deissler, J. Stat. Phys. **40**, 371 (1985); Physica D **18**, 467 (1986); *ibid.* **25**, 233 (1987).
[55] H. W. Müller and M. Tveitereid, Phys. Rev. Lett. **74**, 1582 (1995).
[56] D. G. Aronson and H. F. Weinberger, Adv. Math. **30**, 33 (1978).
[57] G. Dee and J. S. Langer, Phys. Rev. Lett. **50**, 383 (1983).
[58] W. van Saarloos, Phys. Rev. A **37**, 211 (1988); *ibid.* **39**, 6367 (1989).
[59] E. Ben-Jacob, H. Brand, G. Dee, L. Kramer, and J. S. Langer, Physica D **14**, 384 (1985).
[60] J. A. Powell, A. C. Newell, and C. K. R. T. Jones, Phys. Rev. A **44**, 3636 (1991).
[61] Ch. Jung, Diploma thesis, Universität des Saarlandes, Saarbrücken, 1993.
[62] A. V. Getling, *Rayleigh-Bénard Convection* (World Scientific, Singapore, 1996).
[63] We distinguish the propagation direction of TWD's and TWU's by their frequency, $\omega^D = -\omega^U$ for $Re = 0$, and not by their wave vector (as mentioned already in Sec. III B). Thus, k is positive throughout this work and $c_1^D = -c_1^U, c_0^D = -c_0^U$ for $Re = 0$.
[64] E. Kaplan and V. Steinberg, Phys. Rev. Lett. **71**, 3291 (1993).
[65] P. Kolodner, Phys. Rev. A **46**, 6452 (1992).
[66] C. Fütterer, Ph.D. thesis, Universität des Saarlandes, Saarbrücken, 1999.
[67] P. Büchel and M. Lücke, Phys. Rev. E **61**, 3793 (2000).
[68] S. Chandrasekhar, *Hydrodynamic and Hydromagnetic Stability* (Dover, New York, 1981).
[69] J. E. Welch, F. H. Harlow, J. P. Shannon, and B. J. Daly, Los Alamos Scientific Laboratory of the University of California, Report No. LA-3425, 1966 (unpublished); C. W. Hirt, B. D. Nichols, and N. C. Romero, Los Alamos Scientific Laboratory of the University of California, Report No. LA-5852, 1975 (unpublished).
[70] R. Peyret and T. D. Taylor, *Computational Methods in Fluid Flow* (Springer-Verlag, Berlin, 1983).